Pd nanocubes supported on SiW$_{12}$ @Co-ZIF Nanosheets for High-efficiency rupture of ether bonds in model and actual lignin

Haichuan Zhang [a], Zede Yi [a], Shiyu Fu [a,*], Changzhi Li [b], Lucian A. Lucia [c], Qiying Liu [d]

[a] State Key Laboratory of Pulp and Paper Engineering, South China University of Technology, Guangzhou 510640, PR China
[b] CAS Key Laboratory of Science and Technology on Applied Catalysis, Dalian Institute of Chemical Physics, Chinese Academy of Sciences, Dalian 116023, PR China
[c] Department of Forest Biomaterials, College of Natural Resources, North Carolina State University, Raleigh, NC 27695, USA
[d] Key Laboratory of Renewable Energy, Guangzhou Institute of Energy Conversion, Chinese Academy of Sciences, Guangzhou 510640, PR China

ARTICLE INFO

ABSTRACT

A rational design of the intrinsic lattice structure of catalysts is vitally important to address catalytic performance. Herein is reported a top-down synthesis for the fabrication of a bifunctional metallic catalyst. First, palladium nanocubes with (100) lattices planes were synthesized through a shape-control strategy; next, the as-synthesized Pd/Co-ZIF was used as a template for *in-situ* phase reconstruction by a spontaneous phase transformation process in the presence of H$_4$SiW under solvothermal conditions. Ultimately, formation of 3D hierarchical flower-like bimetallic nitride nanosheets (SiW$_{12}$ @Pd/Co-ZIF-NS) were generated because of this process. The SiW$_{12}$ @Pd/Co-ZIF-NS catalyst not only displays excellent catalytic transfer hydrogenolysis for C-O bond cleavage of lignin dimeric substrates, but also maintains superior recycling durability due to an encapsulation phenomenon preventing aggregation. Finally, the resulting nanocomposites exhibit superior activity and good size selectivity toward catalytic transfer hydrogenolysis of the actual lignin substrates to produce a significant amount of low-molecular-weight aromatic compounds.

1. Introduction

Lignin is among the most dominant global polymers principally found in lignocellulosic biomasses. It is derived from three types of phenylpropane units linked by alkyl, aryl, and ether linkages to form a three-dimensional amorphous and irregular polymer [1,2]. Both β-O-4 and α-O-4 ether bonds are the two major linkages which have been identified as primary sites for deconstruction of the polymer [2,3]. Therefore, efficient ether cleavage is considered a pivotal step to attain sustainable aromatic chemicals and high-octane fuel additives. However, conventional catalytic hydrogenolysis depolymerization require harsh conditions and consume inordinate amounts of hydrogen, which decrease process efficiency in terms of energy and carbon balances [4].

Thus, enormous efforts were expenede to address catalytic transfer hydrogenolysis (CTH) of lignin and lignin model compounds which were done by replacing H$_2$ with hydrogen donors or self-hydrogen transfer [1, 5–15]. A typical transfer hydrogenolysis involves two catalytic cycles [1]. Either dehydrogenation or activation of hydrogen donors and the ensuing lignin hydrogenolysis is desired [1]. To that end, varieties of homogeneous and heterogeneous metal catalysts were developed to activate lignin ether bonds [6,9]. However, homogeneous catalysts suffer from tedious separation procedures, equipment corrosion and waste water production [16,17]. In contrast, heterogeneous catalysts prossessing high stability and recyclability would be more applicable for lignin valorization; thus, development of versatile heterogeneous catalysts for selective depolymerization of lignin under mild condition has received extensive attention. Polyoxometalates or heteropoly acids (HPAs) are metal–oxygen cluster anions which display strong Brønsted acidity and attractive redox potentials [18,19]. These make it possible to transfer hydrogen from solvent to substrates in a multiphase catalytic system [20–22]. Metal nanoparticles (NPs) (e.g., Pt, Pd) play a crucial role in hydrogen transfer processes due to their affinity toward hydrogen [23]. Typically, HPAs function as heterogeneous catalysts, but suffer from self-aggregation, which shields catalytic active sites lowering efficiency [24]. Keggin-type HPAs show considerable activity to decomposing biomass, but recovery and recycling of catalysts require improvement [25–27].

Rencently, immobilized HPAs have emerged as a new class of solid acid catalysts with widespread applications in catalysis [24,28–30]. Metal–organic frameworks (MOFs) are one of the most frequently

---

* Corresponding author.
E-mail address: shyfu@scut.edu.cn (S. Fu).

invoked carriers for synthesis of guest@host-type HPA@MOF nano-composites due to tunable catalytic centers and excellent chemical stability [28,31–36]. In particular, MOFs with acid sites and open porous channels not only serve as ideal host matrices to encapsulate metal nanoparticles, but also provide microenvironments to assert control over the catalytic activity and final product selectivity [37,38]. N-rich zeolitic imidazolate frameworks (ZIFs), a cobalt-based MOF, which can realize homogeneous insertion of nitrogen into carbon frameworks have attracted increasing attention because their metal active sites can be tuned by "heterojunction" effects [39–41]. As a result of their size differences compare to bulk MOFs nanohybrids, those ultrathin 2D counterparts reveal more surface metal sites and can thus lower surface energy because of very large surface-to-volume ratios and the quantum-confinement effect resulting in stronger electron transfer ability and higher hydrothermal stability [42–44]. A fast "bottom-up" strategy was proposed for production of 2D nonlayered transition metal carbide/nitride heterostructure nanosheets, which show significant enhancement in performance [45]. For instance, Co-ZIF nano-sheets-derived 2D materials with tailorable dimensionality have been exploited as microwave absorbers [46], lithium−sulfur batteries [47], arsenic (III) removal [48], oxygen evolution reaction (OER) [49–54], and hydrogen evolution reaction (HER) [55], etc. However, 2D MOF nanosheets materials have been rarely explored for hydrogen/hydrogenolysis. It therefore remains challenging to construct an integrated architecture of 2D multicomponent catalysts coupling Pd NCs and HPA and displaying appealing catalytic activity. To this end, unique 3D hierarchical structure composed of 2D ultrathin nanosheets to host Pd NCs, affording a SiW_{12} @Pd/Co-ZIF-NS composite for CTH of lignin were design and fabricated. The synthetic strategy is depicted in Scheme 1: (i) shape-controlled synthesis of Pd nanocubes (NCs); (ii) encapsulation of the catalytically active Pd NCs using the Co-ZIF shell by self-agglomeration; (iii) the as-prepared Pd/Co-ZIF was employed as a template to allow for in situ phase reconstruction by a spontaneous phase transformation in the presence of silicotungstic acid ($H_4SiW_{12}O_{40} \bullet 18 H_2O$, abbreviated as H_4SiW or SiW_{12}) under solvothermolysis, leading to formation of SiW_{12} @Pd/Co-ZIF-NS. These heteropoly acids as precursors may be the first case of a 2 D nanosheet-like structure for Pd NCs immobilization.

2. Experimental section

2.1. Reagents

The following reagents were all of analytical grade and used in our experiments without further purification: methanol, ethanol, 2-propanol, palladium acetate, palladium nitrate, polyvinylpyrrolidone (PVP, Mw = 24 000), L-ascorbic acid (AA), KBr, acetone, Na_2PdCl_4, Co$(NO_3)_2$0.6 H_2O, 2-methylimidazole (2-MIM), tungstosilicic acid hydrate ($H_4SiW_{12}O_{40} \cdot xH_2O$, abbreviated as H_4SiW), benzyl phenyl ether (BPE), phenethyl phenyl ether (PPE), 3-(benzyloxy)phenol, 4-benzyloxy-3-methoxybenzaldehyde, 4-benzyloxy-3-methoxyacetophenone (BMA), 1-(3,4-dimethoxyphenyl)− 2-(2-methoxyphenoxy)propane-1,3-diol, β-hydroxyester, tetrahydrofuran (THF), sodium borohydride, chloroform-*d* ($CDCl_3$), were purchased from Aladdin. Gases used for analysis and for reactions were: Ar (99.999 wt%, Shengying, Guangzhou, China).

2.2. Synthesis of Pd nanocubes

In a typical synthesis of Pd nanocubes [56], 11 mL of an aqueous solution containing polyvinyl pyrrolidone (PVP, 105 mg), L-ascorbic acid (60 mg), KBr (300 mg) and Na_2PdCl_4 (57 mg) was heated at 80 ℃ in ambient conditions under magnetic stirring for 3 h and then cooled to room temperature. Pd nanocubes were collected by centrifugation and washed three times with a water/acetone mixture. The PVP stabilized Pd nanocubes were redispersed in 50 mL of anhydrous methanol.

2.3. Synthesis of Co-ZIF

The Co-ZIF polyhedrons were synthesized according to a previous report with minor variations [28]. Typically, 12 mmol of Co$(NO_3)_2 \cdot 6H_2O$ (Mr: 291.03) 3.49 g was dissolved in 300 mL of methanol. 2-MIM (48 mmol) (Mr: 82.1) 3.94 g was added into a separate container having 300 mL of methanol. The Co$(NO_3)_2$ solution was poured into the 2-MIM solution and stirred for 6 h at room temperature (~25 °C). The purple precipitate was collected by filtration and washed with methanol repeatedly. The as-prepared purple solids were dried at 60 ℃ in a vacuum oven for 12 h to give Co-ZIF.

2.4. Synthesis of Pd/Co-ZIF

Pd/Co-ZIF was prepared according to a previously reported method with modifications [37]. Typically, Co$(NO_3)_2 \cdot 6H_2O$ (291 mg), PVP
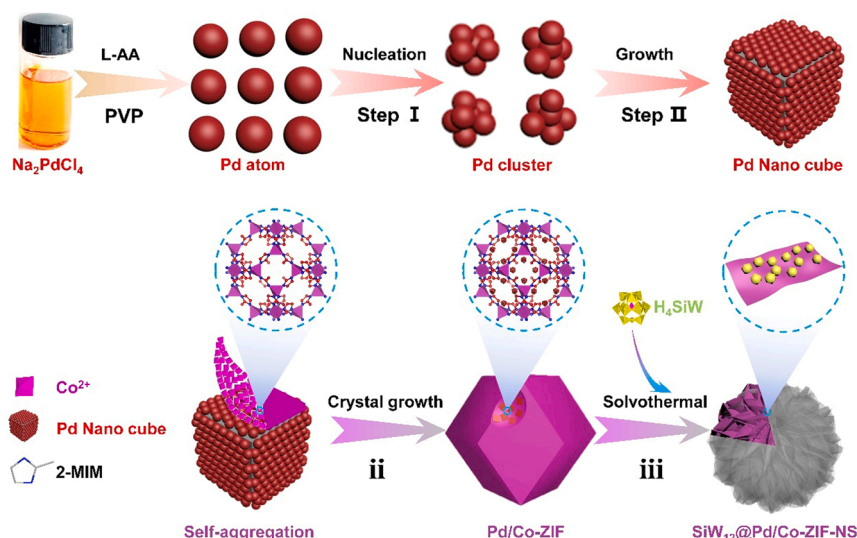
Scheme 1. Preparative routes for SiW_{12} @Pd/Co-ZIF-NS.

(200 mg), and the above PVP modified Pd nanocubes solution (50 mL) were added into methanol (25 mL) and 2-methylimidazole (328 mg) was added into methanol (25 mL). Then, both were mixed and aged at room temperature for 24 h. Afterwards, the dark purple powders obtained by combining the Pd nanocubes and Co-ZIF building blocks was collected by centrifugation and washed three times with methanol to remove unreacted chemicals and dried under vacuum at 60 ℃ overnight.

2.5. Synthesis of SiW$_{12}$ @Pd/Co-ZIF-NS

Synthesis of SiW$_{12}$ @Pd/Co-ZIF-NS was performed in methanol solvent under solvothermal conditions. Typically, 0.1 g of Pd/Co-ZIF was dispersed in 30 mL of methanol and stirred at 30 ℃ for 12 h (solution A). Stirring for too long at this temperance can cause the partial deconstruction of Co^{2+} and 2-MIM, thus giving pore defects. H$_4$SiW (0.05 g, 0.330 mmol) was dissolved in 30 mL of methanol (solution B). Solution B was poured into solution A quickly under constant stirring. The mixture was stirred for 30 min and transferred into a 100 mL Teflon-lined autoclave at 100 ℃ for 6 h. The resulting solid was isolated via centrifugation, and was washed with methanol at least three times. The solid was dried at 60 ℃ in a vacuum oven for 24 h.

2.6. Synthesis of Lignin Model Dimers

1-(3,4-Dimethoxyphenyl)− 2-(2-methoxyphenoxy)propane-1,3-diol (**2**) was synthesized following a literature report [57,58]. Spectra are consistent with reported literature values: ^{1}H NMR (500 MHz, CDCl$_3$) δ 7.06–6.83 (m, 7 H), 4.91 (d, *J* = 4.7 Hz, 1 H), 4.10 (d, *J* = 5.0 Hz, 1 H), 3.96–3.87 (m, 2 H), 3.87 (s, 8 H), 3.68 (dd, *J* = 12.2, 3.4 Hz, 1 H), 3.46 (dd, *J* = 12.3, 5.3 Hz, 1 H), 2.93 (s, 2 H). ^{13}C NMR (126 MHz, CDCl$_3$) δ 152.15, 147.99, 147.43, 145.36, 133.13, 123.78, 121.21, 119.97, 117.39, 111.85, 110.42, 108.19, 85.59, 76.91, 76.28, 76.23, 75.78, 72.23, 63.32, 54.89.

2.7. Characterizations

The powder X-ray diffraction (XRD) patterns of the as-prepared samples were recorded on a PANalytical X′pert Powder diffractometer equipped with Cu Kα X-ray radiation (λ = 1.5406 Å) operated at a tube current of 30 mA and a tube voltage of 40 kV from 5º to 50º.

Fourier transform infrared spectroscopy (FT-IR) was recorded on a Bruker Vertex 70 FT-IR spectrophotometer in the range of 400–4000 cm^{-1}, using the KBr pelleting method.

The scanning electron microscope (SEM) images were taken on a Zeiss Merlin field emission scanning electron microscope and the spatial distribution of the elemental analysis in the samples were measured using scanning electron microscope energy dispersive X-ray spectroscopy (SEM-EDX).

Transmission electron microscopy (TEM) images were obtained on a JEM-2100 F to observe the texture and morphology. Energy-dispersive X-ray spectroscopy (EDX) elemental mapping was recorded on a TEM instrument (JEM-2100 F). The samples for TEM analysis were prepared by dispersing the catalyst powders after grinding in high-purity ethanol (60 min ultrasound treatment), and allowing a drop of the suspension to dry on a carbon-coated copper grid.

We performed a low temperature (−173 °C) electron paramagnetic resonance (EPR) study to detect the presence of nitrogen-oxygen vacancies of catalysts. EPR measurements were conducted with Bruker EMX PLUS EPR spectrometer at 9.330 GHz, using a 100 kHz field modulation frequency and a 3.0 G standard modulation amplitude.

Pyridine-adsorbed FT-IR spectra of the catalyst were obtained on a Nicolet iS50 using KBr pellets in the range of 1400–1700 cm^{-1} to determine acid site types. The amount of Brønsted acid sites was calculated according to the 1540 cm^{-1} characteristic band and the amount of Lewis acid sites was calculated according to the 1450 cm^{-1}

characteristic band [59].

NH$_3$-TPD experiments were performed on a Micromeritics AutoChem1 II 2920 set-up with a TCD detector. In a typical experiment, 80 mg of the sample was placed in a quartz tube and first outgassed under He with flowing 50 mL/min for 1 h at 350 ℃, followed by cooling to 50 ℃ under He flow and subsequent treatment with a flow of 50 mL/min adsorption gas (10% NH$_3$/He) for 60 min. The samples then were flushed with pure He to remove the physisorbed NH$_3$ at the adsorption temperature for 1 h and heated linearly to 400 ℃ at a heating rate of 10 ℃/min. The amounts of acidic sites were determined according to the temperature and the area of the NH$_3$ desorption peaks.

The Brunauer-Emmett-Teller surface area, pore size, and pore volume of the as-prepared samples were measured by N$_2$ adsorption–desorption isotherms using a Micromeritics ASAP 2460 equipment at 77 K. Before testing, all the catalyst samples were outgassed at 120 ℃ for 12 h under 5×10^{-9} Torr vacuum.

XPS measurements were examined on a Kratos Axis Ultra DLD (UK) multi-technique system under ultrahigh vacuum (~5×10^{-9} torr) using a monochromatic Al Kα X-ray source (*hv*=1486.6 eV). All XPS spectra were recorded at an aperture slot of 700 × 300 µm; survey spectra were recorded with a pass energy of 160 eV, and high-resolution spectra were recorded with a pass energy of 40 eV.

The experimental Co *K*-edge XANES spectra were measured using the Synchrotron Radiation Facility (SSRF) (Shanghai, China). Before the analysis at the beamline, samples were pressed into thin sheets with 1 cm in diameter and sealed using Kapton tape film. The XAFS spectra were recorded at room temperature using a 4-channel Silicon Drift Detector (SDD) Bruker 5040. Co *K*-edge extended X-ray absorption fine structure (EXAFS) spectra were recorded in transmission mode. Negligible changes in the line-shape and peak position of Co *K*-edge XANES spectra were observed between two scans taken for a specific sample. The XAFS spectra of these standard samples (Co foil, CoO, Co$_2$O$_3$ and Co$_3$O$_4$) were recorded in transmission mode. Data reduction, data analysis, and EXAFS fitting were performed with the Athena and Artemis programs of the Demeter data analysis packages[60] that utilizes the FEFF6 program[61] to fit the EXAFS data. For Wavelet Transform analysis, the χ(k) exported from Athena was imported into the Hama Fortran code[62].

The palladium and tungsten loadings in the samples were determined by ICP-OES (Optima8300).

TGA was performed on a NETZSCH TG209F3 thermal analyzer with a heating rate of 5 ℃ min^{-1}.

2.8. General procedure for catalytic reactions on lignin and model lignin dimers

The catalytic reactions were performed in a 100 mL batch reactor (SLM-N100). 0.05 mmol of substrate and 100 mg of catalyst were filled in the reactor. Subsequently, the reaction mixture was purged with argon 0.5 h to remove air, heated to required reaction temperature and kept for a desired reaction time under continuous stirring. Afterwards, the reactor was cooled down to room temperature and the excess gas was vented. The catalyst was separated by centrifugation and the final product was analysed by GC/GC-MS. For the reusability studies, the catalyst was separated by centrifugation and washed three times with methanol and dried under vacuum at 80 °C for 4 h before the next use.

The calculations are as follows:

$$\text{Conversion of dimer} = \frac{\text{mole of reacted dimer}}{\text{total mole of dimer}} \times 100\% \tag{1}$$

$$\text{Yield of product} = \frac{\text{mole of product}}{\text{total mole of dimer}} \times 100\% \tag{2}$$

$$\text{Conversion of KP lignin} = \frac{M - M_u}{M} \times 100\% \tag{3}$$

$$\text{Yield of lignin oil (wt\%)} = \frac{\text{Mass of DCM extracted lignin oil}}{\text{Mass of input lignin}} \times 100\% \tag{4}$$

$$\text{Mass of monomer}_x(\text{mg}) = \frac{Mass_{(IS)}}{MW_{(IS)}} \times \frac{Area_x/\text{ECN}_x}{Area_{IS}/\text{ECN}_{(IS)}} \times MW_x \tag{5}$$

$$\text{Yield of lignin monomer (wt\%)} = \frac{\text{Mass of monomer}}{M} \times 100\% \tag{6}$$

M is the mass of initial reactant intake; M_u is the mass of uncoverted reactant; x is the monomer detected by GC-MS; $Mass_{(IS)}$ (mg) is the weight of internal standard dodecane in each analyzed sample; $MW_{(IS)}$ (mg mmol^{-1}) is the molecular weight of internal standard (170.34 mg mmol^{-1}); MW_x (mg mmol^{-1}) is the molecular weight of monomer; $Area_{(IS)}$ is the peak area of internal standard; $Area_x$ is the peak area of monomer; ECNx is the effective carbon number of the lignin monomer molecule; ECN$_{(IS)}$ is the effective carbon number of the internal standard.

3. Results and discussion

3.1. Preparation and characterization of Pd NCs

Pd NCs were synthesized using Pd(O$_2$CCH$_3$)$_2$, Pd(NO$_3$)$_2$, Na$_2$PdCl$_4$ as precursor, while L-ascorbic acid serve as a strong reducing agent in aqueous media. Polyvinylpyrrolidone was a steric stabilizer to protect the Pd NPs from agglomeration [63] and KBr was a capping agent to control the facets of the Pd nanocrystals [64]. The shape-controlled synthesis for Pd crystal growth involved reducing PdCl$_4^{2-}$ to Pd atoms, followed by random localization of Pd atoms to form small Pd clusters ~ 2 nm in diameter [65]. The nucleates underwent facet-directed growth in the presence of Br$^-$, leading to formation of regular NCs, which presented well-defined shapes having an average diameter of ~ 10 nm and narrow size and shape distribution (Figs. 1a-c). For comparison, the Pd precursor affects formation of the nanocubes. When Na$_2$PdCl$_4$ was replaced by Pd(O$_2$CCH$_3$)$_2$ or Pd(NO$_3$)$_2$ in a typical synthesis, nanoparticles in irregular shapes with a broad size distribution were clearly discerned (Fig. S1) possibly due to the poor solubility of Pd(O$_2$CCH$_3$)$_2$ and Pd(NO$_3$)$_2$ in aqueous solution. These investigations clearly reveal types of Pd precursors play a vital role in synthesis of the Pd NCs.
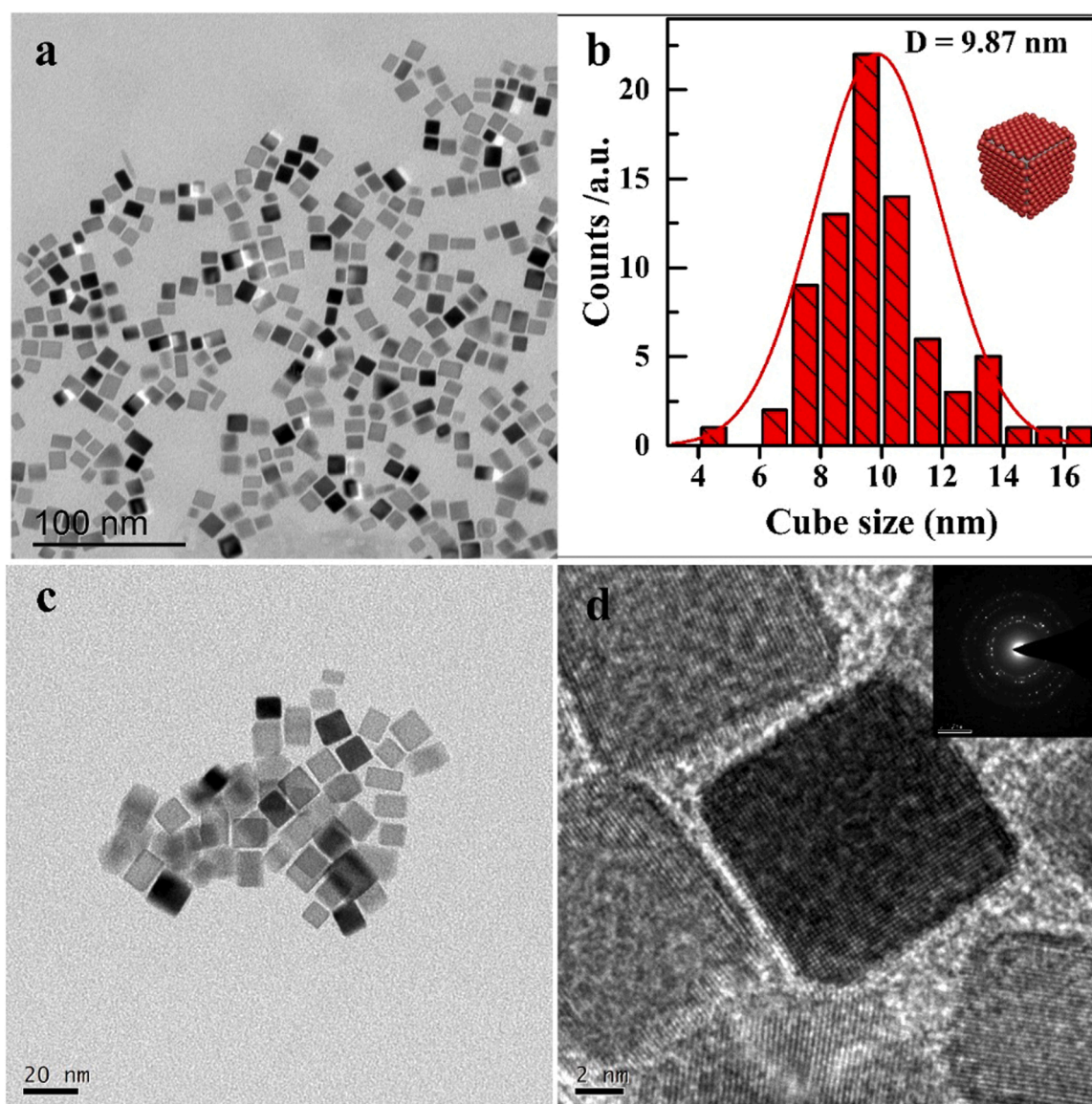

Fig. 1. Morphological characterization of Pd NCs. a) and c) TEM images. b) Size distribution histograms. d) HRTEM image and Fast Fourier transform (FFT) pattern.

High-resolution TEM (HRTEM) photo-images in Fig. 1d reveal clear lattice fringes along the (001) zone axis, where lattice spacings are 1.95 Å, corresponding to the (100) crystal planes of the face-centered cubic (*fcc*) Pd NCs [56,63]. The flat (100) facets of Pd NCs are seeds for MOF growth [38], so that all the Pd NCs are completely covered by

Co-ZIF. The shape of metal NPs also plays a significant role in controlling activity and selectivity because it controls not only the facets, but also proportions of surface atoms at corners, edges, and planes to thus affect catalyses [23]. Pd NCs are one of the most active and widely studied systems [66,67], whilst the synthesis is very challenging. Pd NCs
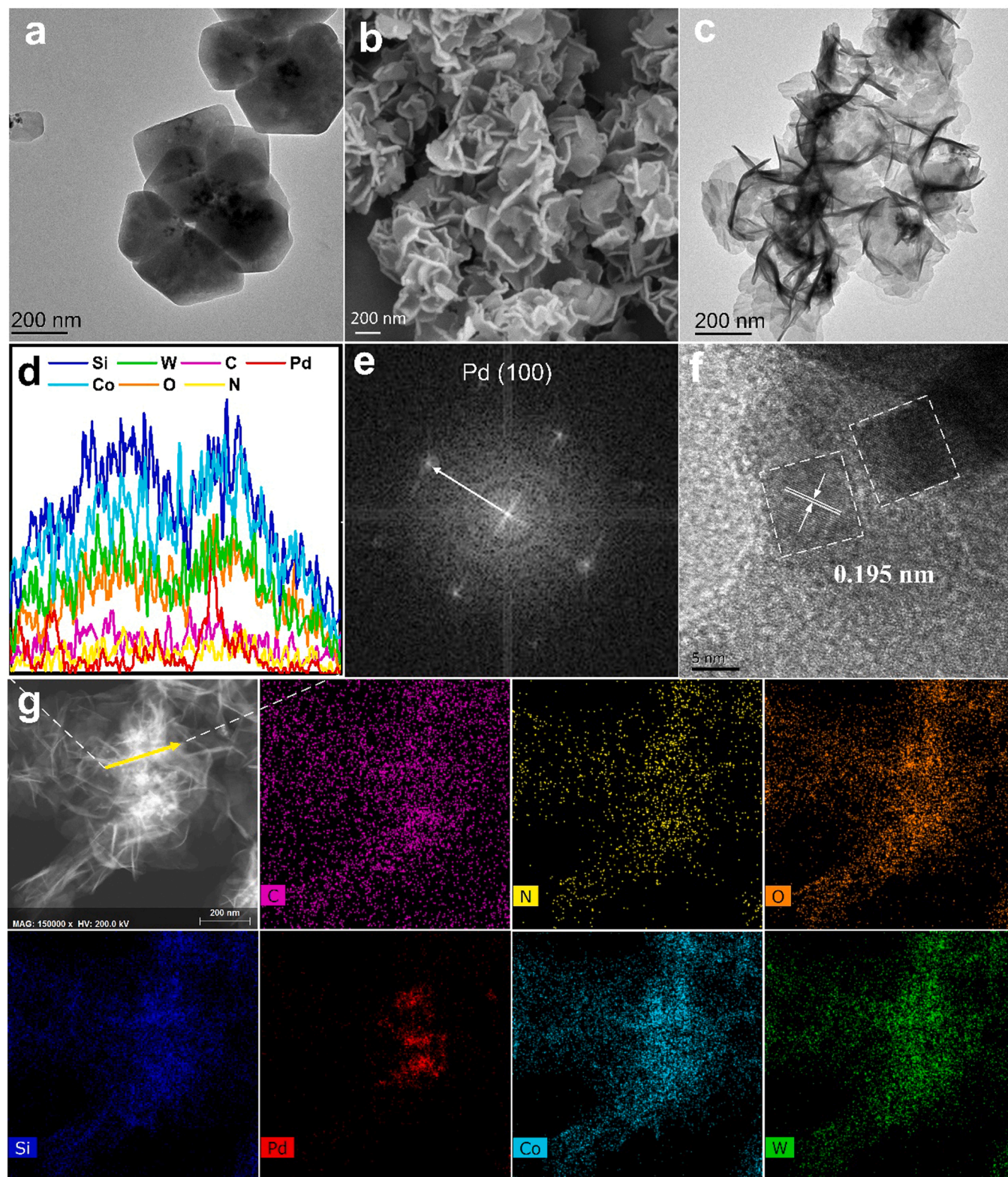
Fig. 2. Electron microscopy characterizations and EDX of SiW$_{12}$ @Pd/Co-ZIF-NS. a) and c) TEM images. b) FESEM image. d) EDX line profiles. e) and f) HRTEM image. g) dark-field STEM image and the corresponding elemental mapping images.

supported on the cavities of MOFs enhance dispersion and stability of metal NPs by preventing them from agglomeration or leaching [68,69].

3.2. Preparation and characterization of SiW$_{12}$ @Pd/Co-ZIF-NS

Stabilization and controlled encapsulation of nanoparticles inside functionalized MOFs have displayed novel chemical and physical performances [70]. Pd/Co-ZIF was synthesized using Pd NCs as crystal seeds for the epitaxial growth of Co-ZIF leading to a deep purple crystal with an average size of 300 nm (Fig. S2a and Fig. S3). The Pd NCs were well encapsulated in Co-ZIF with retention of the rhombododecahedron lattice phase. The subsequent solvothermolysis leads to the enrichment of metal ions on the NCs surface for coordination of H$_4$SiW (Fig. 2a). The increased number of metal ions neighboring the NCs surface induces confined growth of Co-ZIF polyhedrons gradually into the flower-like 2D layered structure seen in Fig. 2c and the corresponding change in color from purple to black (Fig.S2). The Pd NCs cores well stabilized by randomly oriented nanosheets to form a three-dimensional hierarchical superstructure. SEM image revealed similar morphological features with a size of 200–400 nm (Fig. 2b). The open 3D thin film structure of SiW$_{12}$ @Pd/Co-ZIF-NS not only substantially exposes active sites and acidic centers, but improves mass transfer and diffusion of substrates and

products [71]. SiW$_{12}$ @Co-ZIF-NS does not affect crystalline structures, size and distribution of Pd NCs (Fig. 2e-f and Fig. S5), confirming that Pd NPs remain stable during solvothermal treatment. The HRTEM image in Fig. S6 reveals typical fringes of a layered carbon matrix, which possesses considerable electronic conductivity for transferring electrons to metal centers for subsequent reactions [69]. EDX elemental mapping (Fig. 2g) verifies C, N, O, Co, Si, and W were evenly distributed within the nanosheet having a Pd/Co/W atomic ratio ~ 1: 3: 1 (Fig. S4). ICP-OES disclosed an actual Pd loading in SiW$_{12}$ @Pd/Co-ZIF-NS of 2.17 wt% (Table S1) which is slightly lower that of Pd/Co-ZIF (2.71 wt %). The W actual content in SiW$_{12}$ @Pd/Co-ZIF-NS was 22.6 wt%, implying the loading of H$_4$SiW is 29.5 wt%. Furthermore, the EDX line scan reveals C, N, O, Co, Si, and W are very finely dispersed throughout the individual nanocrystal (Fig. 2d). The results demonstrated successful fabrication of SiW$_{12}$ @Pd/Co-ZIF-NS with no noticeable effect on the size and distribution of Pd NCs. Moreover, the 3D hierarchical structure confined cavity and porous nitrogen-doped carbon nanosheet facilitated mass transportation and prevented Pd NCs from leaching.

3.3. Interfacial structure analysis of SiW$_{12}$ @Pd/Co-ZIF-NS

XPS experiments monitored the near surface region chemical states
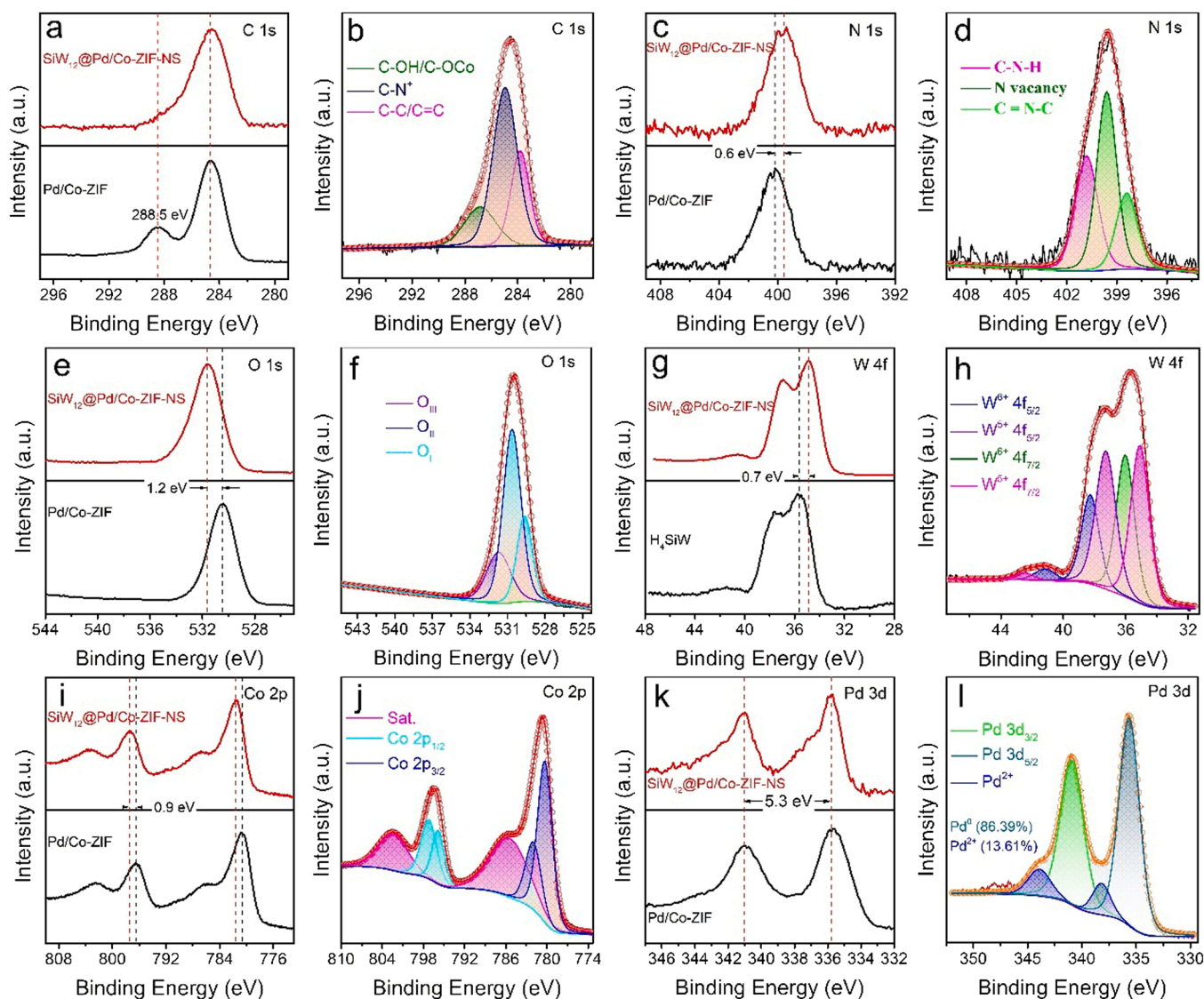

Fig. 3. Interfacial structure analysis of SiW$_{12}$ @Pd/Co-ZIF-NS. a-b) C 1 s high-resolution XPS spectra. c-d) N 1 s high-resolution XPS spectra. e-f) O 1 s high-resolution XPS spectra. g-h) W 4 f high-resolution XPS spectra. i-j) Co 2p high-resolution XPS spectra. k-l) Pd 3d high-resolution XPS spectra.

of as-synthesized composites. Survey spectra (Fig. S7) show that the prepared SiW$_{12}$ @Pd/Co-ZIF-NS contains Co, O, N, Pd, C, Si and W consistent with EDX. In the C 1 s high resolution XPS spectra for Pd/Co-ZIF and SiW$_{12}$ @Pd/Co-ZIF-NS spectra (Fig. 3a), the band energy of C-O (288.5 eV) shifted to lower energy due to weak electronic interaction with the H$_4$SiW Keggin unit attributed to the covalent N-O bonds between H$_4$SiW and Co-ZIF [72]. The high-resolution C 1 s spectrum of SiW$_{12}$ @Pd/Co-ZIF-NS can be deconvoluted into three peaks at 284.8, 285.8 and 286.4 eV (Fig. 3b), which reveal the existence of an sp2 bonded carbon (C-C/C=C), carbon atoms of C-N$^+$, and the epoxy (C-OH/C-OCo), respectively, indicating the presence of an N-doped carbon, hydroxyl groups and oxygen [53].

Compared with Pd/Co-ZIF, the band energy of N 1 s in SiW$_{12}$ @Pd/Co-ZIF-NS exhibited a negative shift by ∼ 0.6 eV (Fig. 3c). The results suggest the rupture of coordinated Co-N bonds leading to a transition from four N-coordination metals to two [72]. The high-resolution N 1 s XPS spectrum confirms three types of N species at 398.4 eV, 399.6 eV, and 400.8 eV (Fig. 3d) corresponding sp^2-hybridized-N (C=N-C), a nitrogen vacancy, and C-N-H [73,74]. The N species not only provide rich anchor sites for stabilizing the Co centers, but also decrease electronic density of Pd NCs as indicated by the Mott−Schottky Effect [40,65].

As shown in Figs. 3e and 3g, the O 1 s peaks shifted to higher binding energy (+1.2 eV), whereas the W 4 f peaks shifted to lower binding energy (−0.7 eV) with concomitant phase transformation. Additionally, the W 4 f and O 1 s core-level peaks are shown in Figs. 3f and 3h. SiW$_{12}$ @Pd/Co-ZIF-NS mainly contains O$^{2−}$ (W-O) and W^{6+} characteristic chemical states assigned from peaks at 530.6 eV, 38.3 eV, and 36.1 eV that matched oxygen species bound to surface oxygen vacancies (O$_{II}$) [75], W^{6+} 4 f$_{5/2}$ and W^{6+} 4 f$_{7/2}$ state, respectively. Another two lower-energy peaks at 35.1 eV and 37.3 eV in W 4 f spectrum belonged to the oxidation state of W^{5+} 4 f$_{7/2}$ and W^{5+} 4 f$_{7/2}$, corresponding to a content of 57.9%, which is much higher than that 42.1% for W^{6+} implying abundant local distortion and variation of the coordination mode for the W–O bond [76]. These results suggest in situ transformation of 3D Co-ZIF nanoparticles to 2D nanosheets with rich surface oxygen vacancies to boost electron transfer ability [75].

As shown in Fig. 3i, the Co 2p peaks in SiW$_{12}$ @Pd/Co-ZIF-NS positively shifts by 0.9 eV relative to that of Co-ZIF due to strong electronic interaction between N and Co in the nanosheet surface. The high-resolution Co spectrum in Fig. 3j reveals the Co^{2+} (795.8 and 780.2 eV) in the coordinatively unsaturated Co-N bonds is transformed to Co^{3+} (797.3 and 782.0 eV) [53,74].
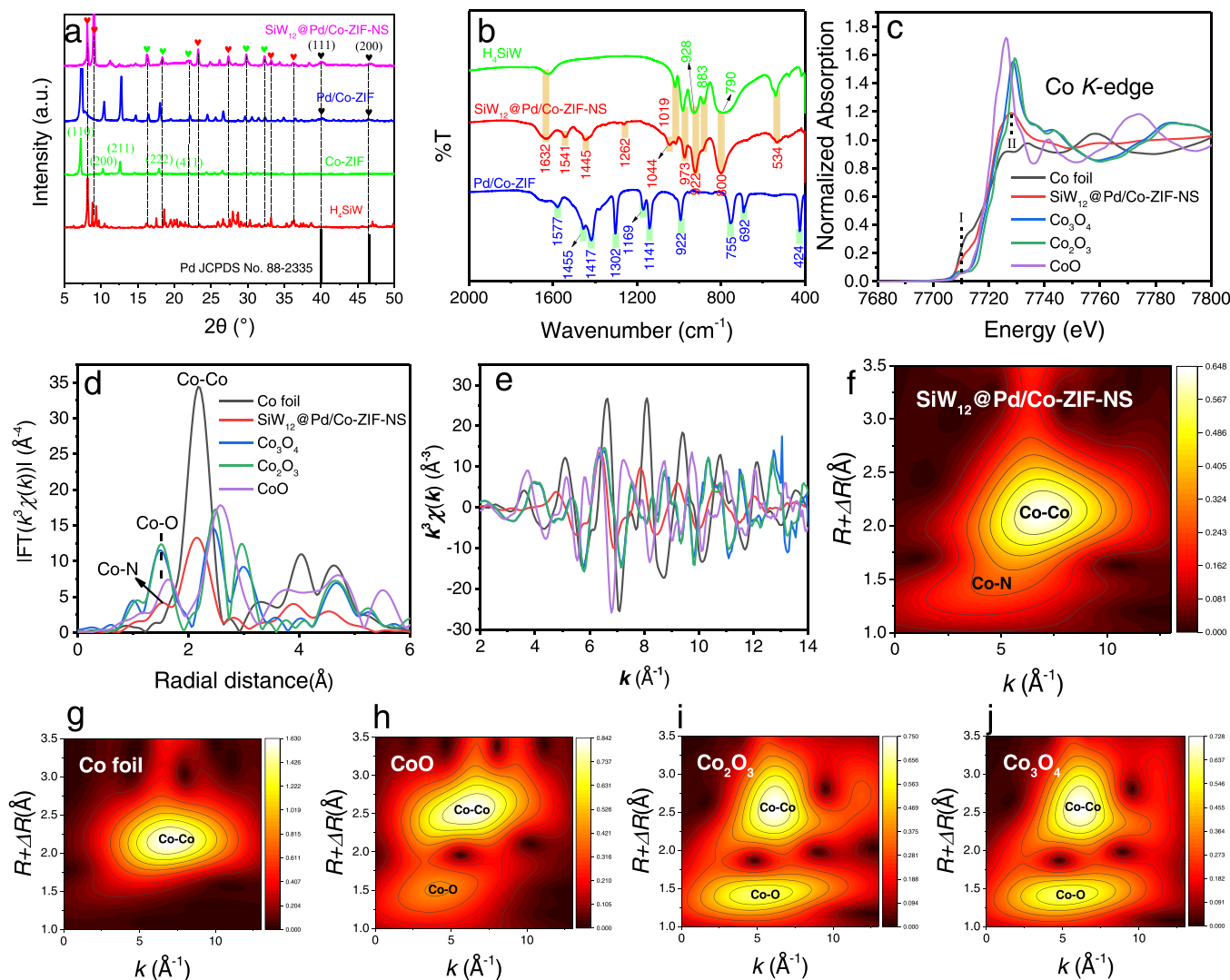
Fig. 4. Fine structure characterizations. a) Powder XRD patterns. b) FT-IR spectra. c) Co K-edge X-ray absorption near edge structure (XANES) spectra. d) Co *K*-edge Fourier transform EXAFS spectra in *R*-space. e) The EXAFS spectra in *k*-space. f)-j) Wavelet transformed (WT) k^2-weighted EXAFS spectra.

The binding energy of metallic Pd located at 335.6 and 340.9 eV with a separation of 5.3 eV in SiW_{12} @Pd/Co-ZIF-NS, exhibits a higher energy shift compared with reported peak positions of Pd nanocubes at 334.2 and 339.4 eV (Figs. 3k and 3l) [56]. This indicates an increase of the bandwidth of Pd resulting in a Pd *d*-band center downshifting; thus, this boosts catalytic activity by weakening the binding affinity between oxygenated species and Pd [77].

XRD characterizations confirm phase transformation from a 3D bulk structure to a nanosheet structure (Fig. 4a). The disappearance of the peak at 7.2° in relation to Co-ZIF in SiW_{12} @Pd/Co-ZIF-NS was found with a concomitant appearance of an outstanding diffraction peak of SiW_{12}. These significant difference between the XRD curves of Co-ZIF and SiW_{12} @Pd/Co-ZIF-NS can be ascribed to the synthetic action of polarization, atomic scattering, destructive interference, and interplane phase shift [48]. The diffraction signals at $2\theta = 40°$ and $2\theta = 46.4°$ for both samples can be assigned to the exposed crystal planes of (111) and (200) for Pd, respectively (JCPDS 88–2335). Besides, in FT-IR spectra (Fig. 4b), the well-defined vibrations at 973 cm^{-1}, 922 cm^{-1} and 800 cm^{-1} further verified the presence of SiW_{12} phase. The characteristic peaks at 800 and 883 cm^{-1} for parent $[SiW_{12}O_{40}]^{4-}$ Keggin structure belong to ($W-O_e-W$) and corner sharing ($W-O_c-W$) groups, and 922 and 1019 cm^{-1} belong to Si–O stretching.[78].

X-ray absorption spectroscopy was then applied to provide further insights into structural information on the valence states and coordination of the central Co atoms in all the samples. Fig. 4c shows the Co *K*-edge XANES spectra and the position of the absorption edge of the SiW_{12} @Pd/Co-ZIF-NS spectrum, which is located close to those of CoO, Co_2O_3 and Co_3O_4, indicates that the electron deficiency in the Co species is predominant in the SiW_{12} @Pd/Co-ZIF-NS phase of the sample. Careful examination of the pre-edge at ~7710 eV suggests the evidently
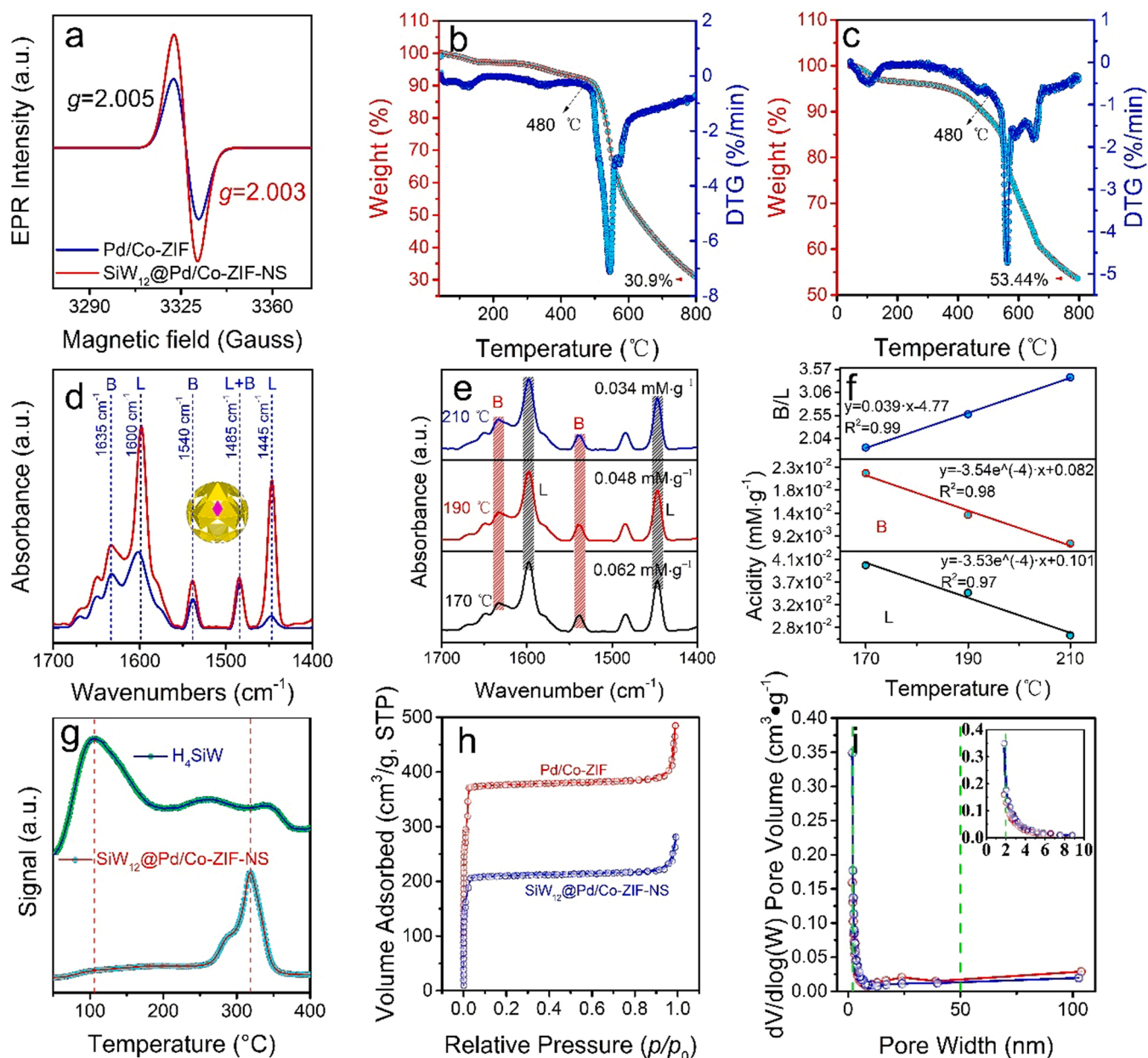
Fig. 5. Performance characterizations of Pd/Co-ZIF and SiW_{12} @Pd/Co-ZIF-NS. a) Low temperature EPR spectra. b) TGA & DTG curves of Pd/Co-ZIF. c) TGA & DTG curves of SiW_{12} @Pd/Co-ZIF-NS. d) Py-IR images (blue colour: H_4SiW; red colour: SiW_{12} @Pd/Co-ZIF-NS), inset shows the crystal of H_4SiW with Lewis acid sites and Brønsted acid sites. e) Py-IR spectra of SiW_{12} @Pd/Co-ZIF-NS at different temperatures. f) B acid, L acid intensity and B/L ratio vs. Temperature in SiW_{12} @Pd/Co-ZIF-NS. g) NH_3-TPD profiles. h) N_2 sorption and desorption isotherms and i) corresponding pore size distribution.

increased 1 s→3d transition peak I in SiW$_{12}$ @Pd/Co-ZIF-NS, signifying rather distorted D$_{4h}$ centrosymmetry of the Co sites. Moreover, the relatively lower height of the peak II intensity implies the presence of a lower oxidation state for the Co atoms, revealing a defective graphene architecture and low-coordinated coordination configuration around the Co atoms.[79] Fourier transform (FT) magnitudes of Co *K*-edge extend X-ray absorption fine structure (EXAFS) of SiW$_{12}$ @Pd/Co--ZIF-NS show a peak at the apparent distance of 2.15 Å with a shoulder ~1.5 Å, which could be fitted by Co-Co and Co-N distances based on the crystal structure of Co-ZIF-NS (Fig. 4d and Table S2). Furthermore, the EXAFS fit in the *k* space provides more detailed information about the coordination environment of such elements (Fig. 4e and Figure S8). The atomic dispersion of the Co was further confirmed by EXAFS wavelet transform (WT) (Fig. 4f), where one intensity maximum at ~5.5 Å^{-1}, in line with the results from the Co *K*-edge XANES. Quantitative structural results were extracted by least-squares EXAFS curve-fitting analysis (Fig. S8 and Table S2, Supporting Information), suggesting that the coordination number of Co atom in SiW$_{12}$ @Pd/Co-ZIF-NS is 2.8 N atoms.

3.4. Performance characterizations of SiW$_{12}$ @Pd/Co-ZIF-NS

The nitrogen-oxygen vacancies of Co-ZIF and SiW$_{12}$ @Pd/Co-ZIF-NS were further confirmed by electron paramagnetic resonance (EPR). As shown in Fig. 5a and Fig. S9, the nanosheet has stronger signal with a g factor of 2.003, indicating the abundant oxygen vacancies in SiW$_{12}$ @Pd/Co-ZIF-NS. The oxygen vacancies could be ascribed to Co^{3+} defect, which provides more lignin adsorption and depolymerization sites, thereby accelerating the breakage of the bonds.

The thermal stability of the precursors and the as-prepared catalyst were evaluated by TGA. Like Pd/Co-ZIF (Fig. 5b), SiW$_{12}$ @Pd/Co-ZIF-NS starts to degrade at ~ 480 °C and presents a total weight loss of ~ 46.7 wt% at 800 °C (Fig. 5c). In contrast, H$_4$SiW undergoes a three-step weight loss compared to SiW$_{12}$ @Pd/Co-ZIF-NS (Fig. S10b). The first weight loss of 10.29% corresponds to dehydration of the inserted water molecules in tungstosilicic acid hydrate followed by gradual destruction and formation of W oxide with increasing temperature [80]. These results imply that the as-prepared catalyst possesses more favorable thermal stability than the parent H$_4$SiW, which may be ascribed to the formation of more stable combinations of SiW$_{12}$ @Co-ZIF-NS composite.

The acidity properties of SiW$_{12}$ @Pd/Co-ZIF-NS were performed by Py-IR and ammonia temperature-programmed desorption (NH$_3$-TPD). Py-IR exhibits the characteristic signals of Lewis acid (1445 cm^{-1}, 1600 cm^{-1}) and Brønsted acid (1540 cm^{-1}, 1635 cm^{-1}) [81]. The adsorption at 1490 cm^{-1} was attributed to pyridine associated with both Lewis acid sites and Brønsted acid sites (Fig. 5d). It appears that the introduction of Co-ZIF significantly increases both Brønsted acid (H$^+$) and Lewis acid (Co^{3+}, Co^{2+}) sites [72]. The density of Lewis acid increased from 13.44 μmolg^{-1} to 204.34 μmolg^{-1}, Brønsted acid increased form 26.05 μmolg^{-1} to 40.19 μmolg^{-1}. As expected, the total amounts of acid sites of SiW$_{12}$ @Pd/Co-ZIF-NS composites decrease with temperature (Figs. 5e and 5 f), and the B/L ratio increases linearly with temperature, which indicates that Pd NCs act to increase the number of Brønsted acid sites with reactivation temperature [82]. Typically, SiW$_{12}$ @Pd/Co-ZIF-NS exhibits a stronger desorption peak recorded at 317 °C (Fig. 5 g) and possesses more total acid sites (4.3 mmolg^{-1}) compared with the H$_4$SiW (1.1 mmolg^{-1}) and reported Co-ZIF (0.32 mmolg^{-1}) [83].

Brunauer–Emmett–Teller (BET) results confirm that the SiW$_{12}$ @Pd/Co-ZIF-NS presents a high porous surface area of 630 m^{2}g^{-1} (Fig. 5 h and Table 1). Meanwhile, SiW$_{12}$ @Pd/Co-ZIF-NS is rich in median pore (5.52 Å) as revealed by the Horvath–Kawazoe method (Fig. 5i). These well-defined porous structures and uniform pore sizes guarantee accessibility of the Pd active sites; in other words, the pores act as a "molecular sieve" for selective catalysis [67]. Based on the above results, SiW$_{12}$ are homogeneously intercalated within the crystal lattice of

Table 1
The results of physical absorption.

| Sample	H$_4$SiW [87]	Pd/Co-ZIF	SiW$_{12}$ @Pd/Co-ZIF-NS
BET (m^2 g^{-1})	9.0	1137	630
Langmuir (m^2 g^{-1})	——	1747	979
External surface area (m^2 g^{-1})[a]	——	38	30
Pore volume (cm^3 g^{-1})[b]	0.02	0.58	0.32
Pore size (Å)[b]	71	5.48	5.52

[a] *t*-Plot method. [b] Horvath–Kawazoe method.

Co-ZIF-NS. The obtained multifunctional catalyst has unique 2D morphology, rich oxygen vacancies, and good cooperation among active components.

### 3.5. Catalytic transfer hydrogenolysis of lignin dimers

Selective cleavage of phenolic ether bonds in lignin while preserving aromatic nuclei remains a huge challenge in sustainable chemistry and renewable energy. Supported Pd catalysts have been observed can catalyze ether cleavage in the presence of H$_2$, but lead to some ring saturation.[84] Synthesized solid catalysts have been employed for selective cleavage of the C$_{\alpha}$-O in lignin dimers in iso-propanol. Reaction parameters such as temperature, reaction time and catalyst dosage on-stream performance for CTH of phenethyl phenyl ether (model lignin dimer **1**) over Pd/Co-ZIF or SiW$_{12}$ @Pd/Co-ZIF-NS is shown in Fig. S14. SiW$_{12}$ @Pd/Co-ZIF-NS shows a considerably better reaction activity by comparison with Pd/Co-ZIF. The optimal conditions determined were as follows: a reaction temperature of 190 °C, reaction time of 8 h and catalyst dosage of 100 mg. Under the catalytic condition, it was observed that model lignin dimer **1** underwent selective C-O bond cleavage at the aliphatic carbon to afford ethylbenzene (**1a**) and phenol (**1b**) in 87% and 93% yield, respectively (Scheme 2). It was noted that hydrogenolysis of **1** also occurred with a mixture of Pd/Co-ZIF and H$_4$SiW; however, a much lower conversion of 25.5% was found under the same conditions, suggesting a clear synergistic effect of acid sites and metal sites on SiW$_{12}$ @Pd/Co-ZIF-NS for hydrogenolysis of **1**.

Moreover, the α-O-4 model compound having C$_{ary}$-O and C$_{alky}$-O bonds were reductively cleaved by SiW$_{12}$ @Pd/Co-ZIF-NS. As shown in Scheme 3, compound **3** was cleaved to form toluene in high yields, which are much better than reported yield under relatively mild conditions (Table S3) [9,12,85]. In addition, α-O-4 model compounds **5** (4-benzyloxy-3-methoxybenzaldehyde) was fragmented to corresponding monomers benzene, toluene, vanillin, 2-methoxy-4-methylphenol and guaiacol in good yields (see Scheme 4). In contrast, the control experiment using Pd/Co-ZIF and H$_4$SiW as co-catalysts afforded only trace amounts of **5a** and **5b**. To further explore versatility, the cleavage of a more complex β-O-4 model compound **2**, 1-(3, 4-dimethoxyphenyl)− 2-(2-methoxyphenoxy) propane-1,3-diol, with α-hydroxyl, γ-hydroxyl and methoxy substituents was investigated (Scheme 5A). The results showed that **2** underwent a tandem reaction of hydrogenolysis and hydrodeoxygenation (HDO) to furnish ethyl-substituted arene (**2a**), propylarene (**2b**) and o-hydroxyanisole (**2c**) in 66%, 31% and 82% yields, respectively. Monitoring the fragmentation of **4** and **6** further evidence that HDO is occurred in the presence of SiW$_{12}$ @Pd/Co-ZIF-NS. Over the 8 h of the reaction, 99% conversion was observed; toluene formed to reach 73% and 78% yields in Schemes 5B and 5C, respectively.

Meanwhile, SiW$_{12}$ @Pd/Co-ZIF-NS showed dramatically improved hydrogenolysis with respect to previously reported monometallic and bimetallic catalysts (Table S3). The higher catalytic efficiency of SiW$_{12}$ @Pd/Co-ZIF-NS as compared to the Pd/Co-ZIF+H$_4$SiW is probably attributed to faster mass diffusion and good cooperation among the active components (Fig. 6a). Based on these findings and results from experiments, a reaction mechanism was proposed as shown in Fig. 6b. At
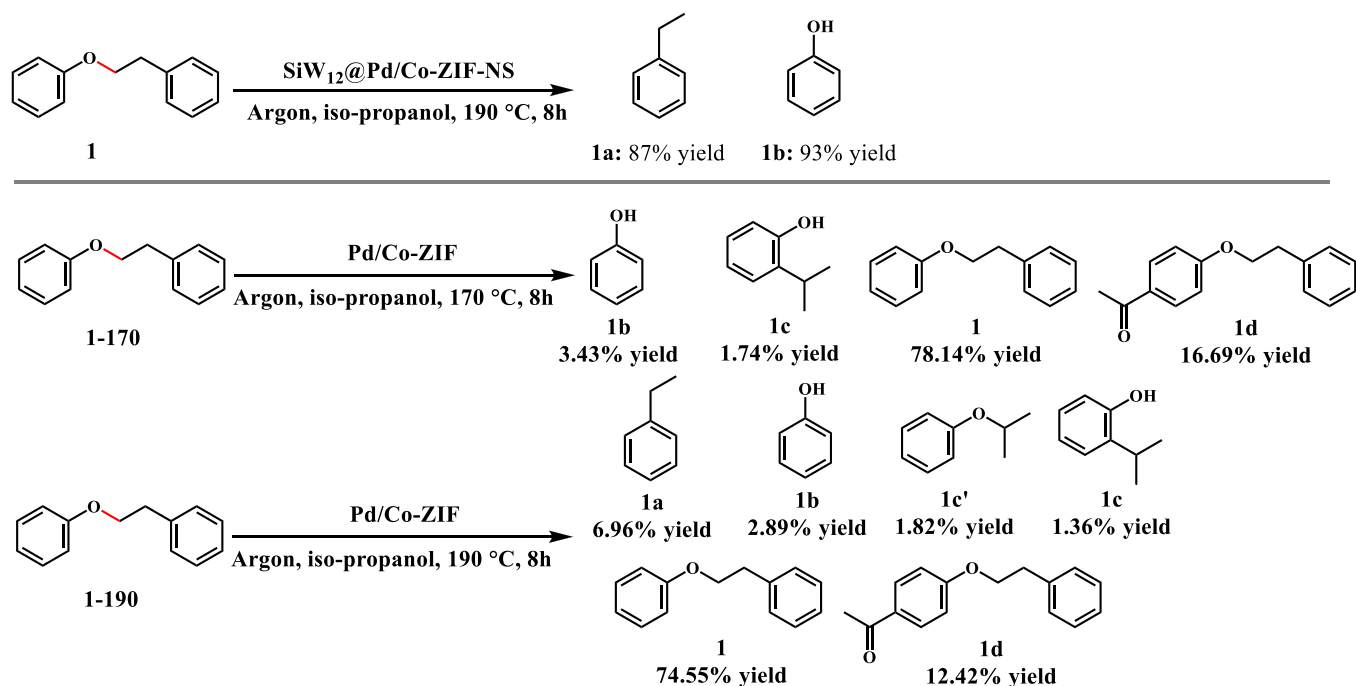
Scheme 2. Catalytic C−O bond cleavage of β-O-4 model lignin dimers. Reaction conditions: 0.05 mmol of substrate **1**, 100 mg of catalysts, 50 mL of iso-propanol, 1 atm of Argon, 170, 190 ℃, 8 h, 600 rpm.
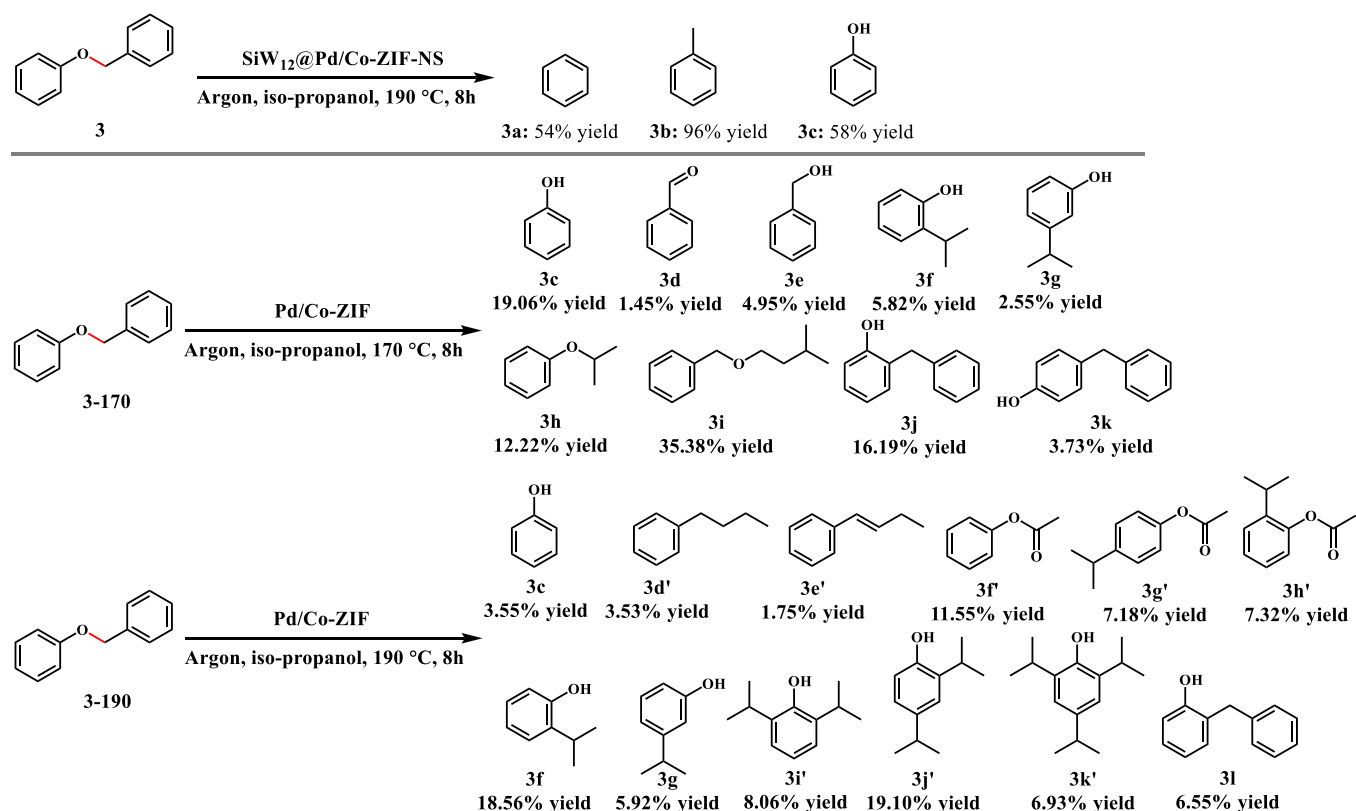
Scheme 3. Catalytic C−O bond cleavage of α-O-4 model lignin dimers. Reaction conditions: 0.05 mmol of substrate **3**, 100 mg of catalysts, 50 mL of iso-propanol, 1 atm of Argon, 170, 190 ℃, 8 h, 600 rpm.

the initial stage, iso-propanol decomposes on the SiW$_{12}$ @Pd/Co-ZIF-NS surface into H$_2$, which is confirmed by GC (TCD detector) of collected gas from the reaction. As we know, the hydrogen in the hydroxyl group (-OH) of iso-propanol is active (H*), which can absorb to the Pd NCs

surface and spills over. Thereafter, H$^+$ from Brønsted acid sites of SiW$_{12}$ @Pd/Co-ZIF-NS and H* are transferred to electron rich O and electron deficient N of nitro group, respectively. Subsequent reduction of the phenyl Brønsted acid species by the Pd-H species would afford the
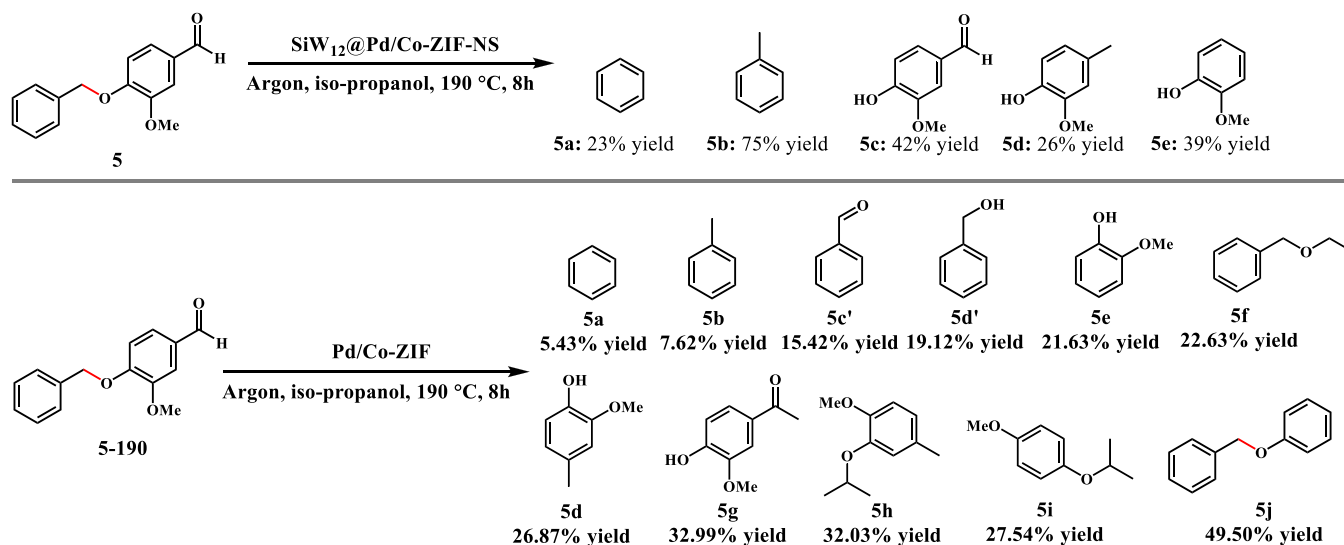
Scheme 4. Investigation of HDO in compound **5** by catalytic transfer hydrogenation. Reaction conditions: 0.05 mmol of substrate **5**, 100 mg of catalysts, 50 mL of iso-propanol, 1 atm of Argon, 190 ℃, 8 h, 600 rpm.

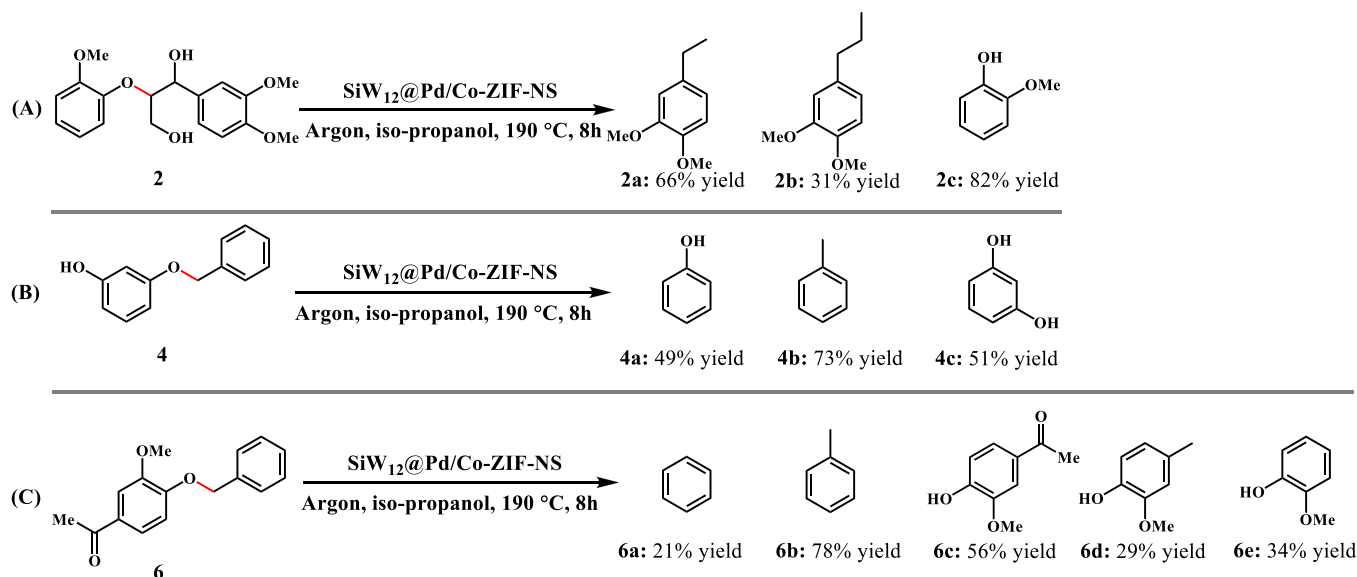**Scheme 5.** Investigation of CTH process using more complex lignin model compounds. Reaction conditions: 0.05 mmol of substrate, 100 mg of SiW$_{12}$ @Pd/Co-ZIF-NS, 50 mL of iso-propanol, 1 atm of Argon, 190 ℃, 8 h, 600 rpm.

corresponding arene. This indicates that hydrogenolysis and hydrodeoxygenation co-exist in this reaction. Motivated by these results, the catalytic hydrogenolysis of an actual eucalyptus kraft lignin (EKL) was tested. Full conversion and total quantified monomer yield of 41 wt% were obtained under similar conditions (Scheme 6). It is near the maximum attainable yield based on complete ether cleavage (45–50%) [86]. It was found to be highly selective towards $C_7 \sim C_9$ products thanks to active sites introduction in the MOF composite and HPAs precursor to produce a 3D hierarchical structure with unique 2D bimetallic nitride nanosheets and rich oxygen vacancies and good cooperation among the active components.

3.6. Reusability and stability

After all reactions, SiW$_{12}$ @Pd/Co-ZIF-NS was readily separated by centrifugation and recycled in four successive reactions of model lignin dimers virtually without any decay in catalytic activity (Fig. 6c). Encapsulation of Pd NCs within Co-ZIF nanosheet prevents aggregation

and leaching of NCs and thus results in superior catalytic recyclability [68,69]. Furthermore, the TEM (Fig. S11) and EDX mapping (Fig. S12) reveal uniform distribution of Pd NCs and elements in catalyst sample after four runs. The Pd content of the SiW$_{12}$ @Pd/Co-ZIF-NS was determined to be 2.10 wt% after four runs (Table S1) demonstrating the content of Pd NCs is consistent during the catalysis. On the contrary, the conversion activity of control catalyst sharply dropped (<25%) after being subjected to four consecutive runs. The above results unambiguously demonstrate that SiW$_{12}$ @Pd/Co-ZIF-NS can effectively reduce migration and agglomeration to greatly improves catalytic activity and recycling stability.

4. Conclusions

In summary, an effective strategy to construct a novel Pd NCs loaded bimetallic nitrides of 3D hierarchical flower-like superstructure composed of 2D ultrathin nanosheets using silicotungstic acid as precursor was demonstrated for the first time. The as-prepared SiW$_{12}$ @Pd/
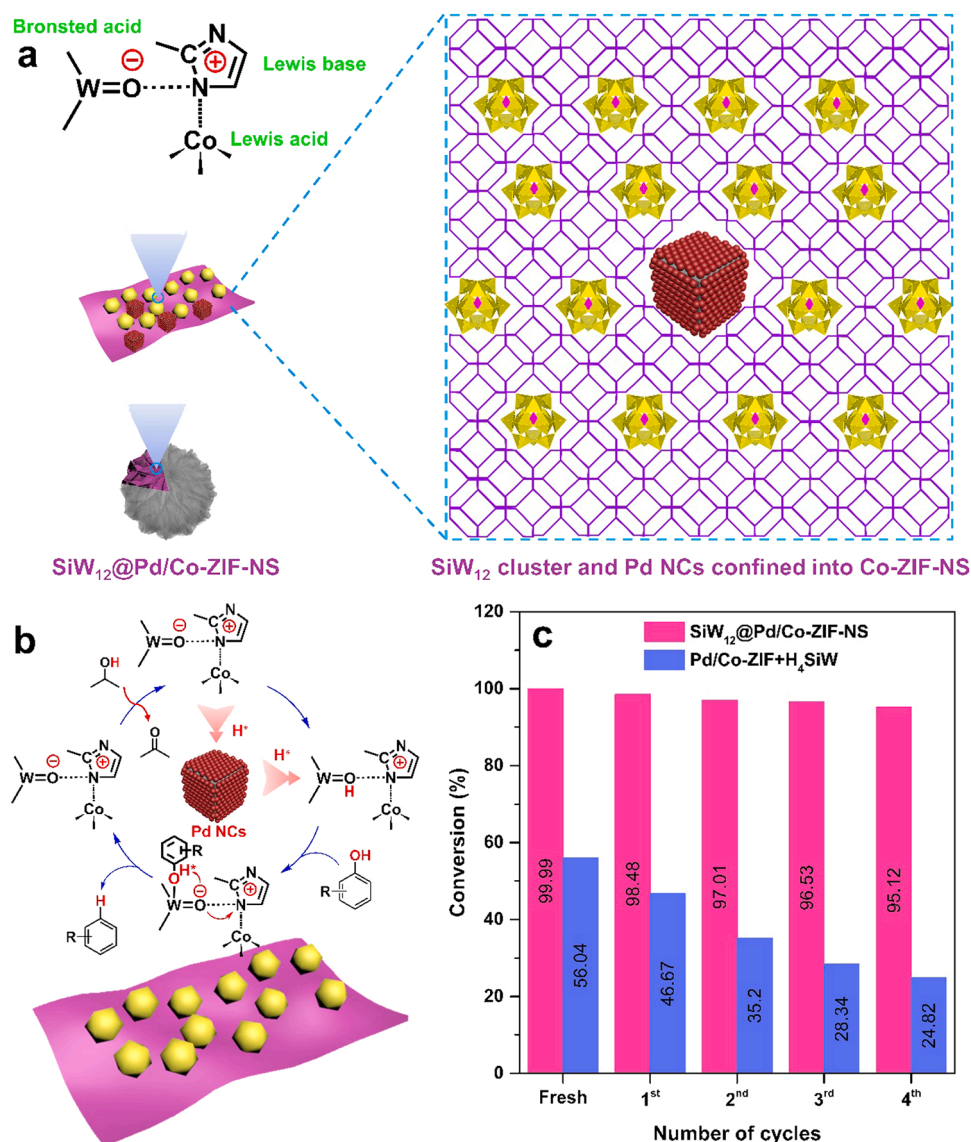
Fig. 6. a) Plausible structure of acid–base SiW$_{12}$ @Pd/Co-ZIF-NS. b) Possible mechanism for the SiW$_{12}$ @Pd/Co-ZIF-NS catalyzed CTH reactions. c) Results of catalytic cycling, reaction conditions: 0.05 mmol benzyl phenyl ether, 100 mg catalyst, 50 mL isopropanol, 190 °C, 8 h, 600 rpm.
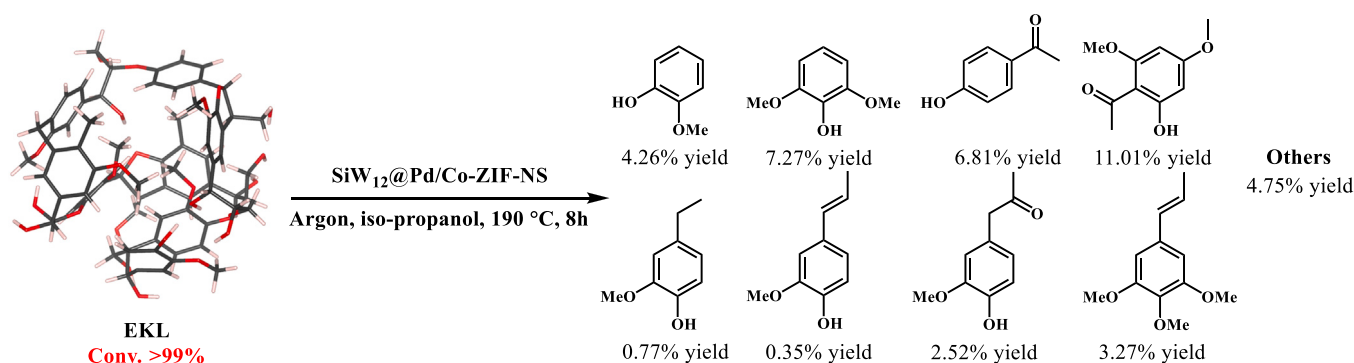
Scheme 6. Catalytic kraft lignin depolymerization. Reaction conditions: 0.05 mmol of substrate, 100 mg of SiW$_{12}$ @Pd/Co-ZIF-NS, 50 mL of iso-propanol, 1 atm of Argon, 190 ℃, 8 h, 600 rpm.

Co-ZIF-NS multifunctional catalyst has unique 2D morphology, rich oxygen vacancies, and good cooperation among the active components. As a result, the remarkable CTH activity toward lignin dimers C-O bond cleavage and actual lignin was shown with nearly full conversion under relatively mild conditions. Such catalytic performance demonstrates significant advantages of the as-prepared hierarchical porous structure with sufficient atomic doping to provide a high density of accessible active sites for improved mass and charge transport. This work can lead

to future design and construction of 3D hierarchical flower-like bimetallic heteroatoms nanosheets ($M_{1x}M_{2y}$-H-3DHFLNs) by applying heteropoly acids as precursors; in essence, M_1 and M_2 represent metallic atoms; H represents heteroatom, e.g., N, P, S, and so on to stabilizes Pd NCs.

CRediT authorship contribution statement

Haichuan Zhang: Conceptualization, Methodology, Data curation, Writing – original draft. **Zede Yi:** Data curation. **Shiyu Fu:** Conceptualization, Methodology, Resources, Writing – review & editing, Funding acquisition. **Changzhi Li:** Writing – review & editing. **Lucian A. Lucia:** Writing – review & editing. **Qiying Liu:** Review.

Declaration of Competing Interest

The authors declare that they have no known competing financial interests or personal relationships that could have appeared to influence the work reported in this paper.

Data Availability

The authors do not have permission to share data.

Acknowledgements

Appendix A. Supporting information

Supplementary data associated with this article can be found in the online version at doi:10.1016/j.apcatb.2022.122128.

References

[1] J. Zhang, Catalytic transfer hydrogenolysis as an efficient route in cleavage of lignin and model compounds, Green. Energy Environ. 3 (2018) 328–334.

[2] M. Wang, F. Wang, Catalytic scissoring of lignin into aryl monomers, Adv. Mater. 31 (2019) 1901866.

[3] X. Wang, R. Rinaldi, Solvent effects on the hydrogenolysis of diphenyl ether with raney nickel and their implications for the conversion of lignin, ChemSusChem 5 (2012) 1455–1466.

[4] C. Li, X. Zhao, A. Wang, G.W. Huber, T. Zhang, Catalytic transformation of lignin for the production of chemicals and fuels, Chem. Rev. 115 (2015) 11559–11624.

[5] P. Ferrini, R. Rinaldi, Catalytic biorefining of plant biomass to non-pyrolytic lignin bio-oil and carbohydrates through hydrogen transfer reactions, Angew. Chem. Int. Ed. 53 (2014) 8634–8639.

[6] F. Gao, J.D. Webb, H. Sorek, D.E. Wemmer, J.F. Hartwig, Fragmentation of lignin samples with commercial Pd/C under ambient pressure of hydrogen, ACS Catal. 6 (2016) 7385–7392.

[7] N. Luo, M. Wang, H. Li, J. Zhang, T. Hou, H. Chen, X. Zhang, J. Lu, F. Wang, Visible-light-driven self-hydrogen transfer hydrogenolysis of lignin models and extracts into phenolic products, ACS Catal. 7 (2017) 4571–4580.

[8] J.-w Zhang, G.-p Lu, C. Cai, Self-hydrogen transfer hydrogenolysis of β-O-4 linkages in lignin catalyzed by MIL-100(Fe) supported Pd–Ni BMNPs, Green. Chem. 19 (2017) 4538–4543.

[9] L. Jiang, H. Guo, C. Li, P. Zhou, Z. Zhang, Selective cleavage of lignin and lignin model compounds without external hydrogen, catalyzed by heterogeneous nickel catalysts, Chem. Sci. 10 (2019) 4458–4468.

[10] S.T. Nguyen, P.R.D. Murray, R.R. Knowles, Light-driven depolymerization of native lignin enabled by proton-coupled electron transfer, ACS Catal. 10 (2020) 800–805.

[11] L. Li, L. Dong, D. Li, Y. Guo, X. Liu, Y. Wang, Hydrogen-free production of 4-alkylphenols from lignin via self-reforming-driven depolymerization and hydrogenolysis, ACS Catal. 10 (2020) 15197–15206.

[12] C. Chen, D. Wu, P. Liu, J. Li, H. Xia, M. Zhou, J. Jiang, Eco-friendly preparation of ultrathin biomass-derived Ni3S2-doped carbon nanosheets for selective hydrogenolysis of lignin model compounds in the absence of hydrogen, Green. Chem. 23 (2021) 3090–3103.

[13] X. Shen, C. Zhang, B. Han, F. Wang, Catalytic self-transfer hydrogenolysis of lignin with endogenous hydrogen: road to the carbon-neutral future, Chem. Soc. Rev. 51 (2022) 1608–1628.

[14] Y. Liu, C. Li, W. Miao, W. Tang, D. Xue, J. Xiao, T. Zhang, C. Wang, Rhodium-terpyridine catalyzed redox-neutral depolymerization of lignin in water, Green. Chem. 22 (2020) 33–38.

[15] Y. Liu, C. Li, W. Miao, W. Tang, D. Xue, C. Li, B. Zhang, J. Xiao, A. Wang, T. Zhang, C. Wang, Mild redox-neutral depolymerization of lignin with a binuclear Rh complex in water, ACS Catal. 9 (2019) 4441–4447.

[16] A. Pineda, A.F. Lee, Heterogeneously catalyzed lignin depolymerization, Appl. Petrochem. Res. 6 (2016) 243–256.

[17] R. Zhong, B.F. Sels, Sulfonated mesoporous carbon and silica-carbon nanocomposites for biomass conversion, Appl. Catal. B: Environ. 236 (2018) 518–545.

[18] I.V. Kozhevnikov, Advances in catalysis by heteropolyacids, Russian, Chem. Rev. 56 (1987) 811–825.

[19] I.V. Kozhevnikov, Heterogeneous acid catalysis by heteropoly acids: approaches to catalyst deactivation, J. Mol. Catal. A: Chem. 305 (2009) 104–111.

[20] J. Feng, L. Tong, Y. Zhu, J. Jiang, C. Hse, H. Pan, Efficient utilization and conversion of whole components in waste biomass with one-pot-oriented liquefaction, ACS Sustain. Chem. Eng. 7 (2019) 18142–18152.

[21] W. Liu, W. You, W. Sun, W. Yang, A. Korde, Y. Gong, Y. Deng, Ambient-pressure and low-temperature upgrading of lignin bio-oil to hydrocarbons using a hydrogen buffer catalytic system, Nature, Energy 5 (2020) 759–767.

[22] S. Li, Q. Ma, W. Zhong, X. Zhao, X. Wei, X. Zhang, Q. Liu, C. Wang, L. Ma, Q. Zhang, One-pot hydrodeoxygenation of bioderived furans into octane at low temperatures via an octanediol route, Green. Chem. 23 (2021) 4741–4752.

[23] H. Zhang, M. Jin, Y. Xiong, B. Lim, Y. Xia, Shape-controlled synthesis of Pd nanocrystals and their catalytic applications, Acc. Chem. Res. 46 (2013) 1783–1794.

[24] J. Li, Z. Yang, S. Li, Q. Jin, J. Zhao, Review on oxidative desulfurization of fuel by supported heteropolyacid catalysts, J. Ind. Eng. Chem. 82 (2020) 1–16.

[25] B. OpdeBeeck, J. Geboers, S. VandeVyver, J. VanLishout, J. Snelders, W.J. J. Huijgen, C.M. Courtin, P.A. Jacobs, B.F. Sels, Conversion of (Ligno)cellulose feeds to isosorbide with heteropoly acids and Ru on carbon, ChemSusChem 6 (2013) 199–208.

[26] H. Zhang, H. Zhang, S. Tian, S. Fu, Deconstruction of biomass into lignin oil and platform chemicals over heteropoly acids with carbon-supported palladium as a hybrid catalyst under mild conditions, Bioresour. Technol. 341 (2021), 125848.

[27] J. Zhong, J. Pérez-Ramírez, N. Yan, Biomass valorisation over polyoxometalate-based catalysts, Green. Chem. 23 (2021) 18–36.

[28] C. Chen, A. Wu, H. Yan, Y. Xiao, C. Tian, H. Fu, Trapping $[PMo_{12}O_{40}]^{3-}$ clusters into pre-synthesized ZIF-67 toward Mo_xCo_xC particles confined in uniform carbon polyhedrons for efficient overall water splitting, Chem. Sci. 9 (2018) 4746–4755.

[29] J. Li, Z. Yang, G. Hu, J. Zhao, Heteropolyacid supported MOF fibers for oxidative desulfurization of fuel, Chem. Eng. J. 388 (2020), 124325.

[30] J. Amaya, S. Moreno, R. Molina, Heteropolyacids supported on clay minerals as bifunctional catalysts for the hydroconversion of decane, Appl. Catal. B: Environ. 297 (2021), 120464.

[31] C.-Y. Sun, S.-X. Liu, D.-D. Liang, K.-Z. Shao, Y.-H. Ren, Z.-M. Su, Highly stable crystalline catalysts based on a microporous metal−organic framework and polyoxometalates, J. Am. Chem. Soc. 131 (2009) 1883–1888.

[32] C.T. Buru, P. Li, B.L. Mehdi, A. Dohnalkova, A.E. Platero-Prats, N.D. Browning, K. W. Chapman, J.T. Hupp, O.K. Farha, Adsorption of a catalytically accessible polyoxometalate in a mesoporous channel-type metal–organic framework, Chem. Mater. 29 (2017) 5174–5181.

[33] S. Mukhopadhyay, J. Debgupta, C. Singh, A. Kar, S.K. Das, A. Keggin, Polyoxometalate shows water oxidation activity at neutral pH: POM@ZIF-8, an efficient and robust electrocatalyst, Angew. Chem. Int. Ed. 57 (2018) 1918–1923.

[34] Q.Y. Li, L. Zhang, Y.X. Xu, Q. Li, H. Xue, H. Pang, Smart Yolk/Shell ZIF-67@POM hybrids as efficient electrocatalysts for the oxygen evolution reaction, ACS Sustain. Chem. Eng. 7 (2019) 5027–5033.

[35] L. Chen, X. Zhang, J. Zhou, Z. Xie, Q. Kuang, L. Zheng, A nano-reactor based on PtNi@metal–organic framework composites loaded with polyoxometalates for hydrogenation–esterification tandem reactions, Nanoscale 11 (2019) 3292–3299.

[36] V.K. Abdelkader-Fernández, D.M. Fernandes, S.S. Balula, L. Cunha-Silva, C. Freire, Oxygen evolution reaction electrocatalytic improvement in POM@ZIF nanocomposites: a bidirectional synergistic effect, ACS Appl. Energy Mater. 3 (2020) 2925–2934.

[37] A. Zhou, R.-M. Guo, J. Zhou, Y. Dou, Y. Chen, J.-R. Li, Pd@ZIF-67 derived recyclable Pd-based catalysts with hierarchical pores for high-performance heck reaction, ACS Sustain. Chem. Eng. 6 (2018) 2103–2111.

[38] Y. Chen, O. Sakata, Y. Nanba, L.S.R. Kumara, A. Yang, C. Song, M. Koyama, G. Li, H. Kobayashi, H. Kitagawa, Electronic origin of hydrogen storage in MOF-covered palladium nanocubes investigated by synchrotron X-rays, Commun. Chem. 1 (2018) 61.

[39] X. Xu, Y. Li, Y. Gong, P. Zhang, H. Li, Y. Wang, Synthesis of palladium nanoparticles supported on mesoporous N-doped carbon and their catalytic ability for biofuel upgrade, J. Am. Chem. Soc. 134 (2012) 16987–16990.

[40] X.-H. Li, M. Antonietti, Metal nanoparticles at mesoporous N-doped carbons and carbon nitrides: functional Mott–Schottky heterojunctions for catalysis, Chem. Soc. Rev. 42 (2013) 6593–6604.

[41] W. Yao, J. Chen, Y. Wang, R. Fang, Z. Qin, X. Yang, L. Chen, Y. Li, Nitrogen-doped carbon composites with ordered macropores and hollow walls, Angew. Chem. Int. Ed. 60 (2021) 23729–23734.

[42] Z. Chen, Y. Ha, H. Jia, X. Yan, M. Chen, M. Liu, R. Wu, Oriented transformation of Co-LDH into 2D/3D ZIF-67 to achieve Co–N–C hybrids for efficient overall water splitting, Adv. Energy Mater. 9 (2019) 1803918.

[43] S. Feng, M. Bu, J. Pang, W. Fan, L. Fan, H. Zhao, G. Yang, H. Guo, G. Kong, H. Sun, Z. Kang, D. Sun, Hydrothermal stable ZIF-67 nanosheets via morphology regulation strategy to construct mixed-matrix membrane for gas separation, J. Membr. Sci. 593 (2020), 117404.

[44] S. Yuan, J. Peng, B. Cai, Z. Huang, A.T. Garcia-Esparza, D. Sokaras, Y. Zhang, L. Giordano, K. Akkiraju, Y.G. Zhu, R. Hübner, X. Zou, Y. Román-Leshkov, Y. Shao-Horn, Tunable metal hydroxide–organic frameworks for catalysing oxygen evolution, Nat. Mater. 21 (2022) 673–680.

[45] Z. Kou, T. Wang, Q. Gu, M. Xiong, L. Zheng, X. Li, Z. Pan, H. Chen, F. Verpoort, A. K. Cheetham, S. Mu, J. Wang, Rational design of holey 2D nonlayered transition metal carbide/nitride heterostructure nanosheets for highly efficient water oxidation, advanced energy, Materials 9 (2019) 1803768.

[46] L. Wang, B. Wen, X. Bai, C. Liu, H. Yang, Facile and green approach to the synthesis of zeolitic imidazolate framework nanosheet-derived 2D Co/C composites for a lightweight and highly efficient microwave absorber, J. Colloid Interface Sci. 540 (2019) 30–38.

[47] S. Feng, H. Zhong, J. Song, C. Zhu, P. Dong, Q. Shi, D. Liu, J. Li, Y.-C. Chang, S. P. Beckman, M.-k Song, D. Du, Y. Lin, Catalytic activity of Co–X (X = S, P, O) and its dependency on nanostructure/chemical composition in lithium–sulfur batteries, ACS Appl. Energy Mater. 1 (2018) 7014–7021.

[48] P. Zhao, M. Jian, R. Xu, Q. Zhang, C. Xiang, R. Liu, X. Zhang, H. Liu, Removal of arsenic(iii) from water by 2D zeolitic imidazolate framework-67 nanosheets, Environ. Sci.: Nano 7 (2020) 3616–3626.

[49] T. Zhang, J. Du, H. Zhang, C. Xu, In-situ growth of ultrathin ZIF-67 nanosheets on conductive Ti@TiO$_2$/CdS substrate for high-efficient electrochemical catalysis, Electrochim. Acta 219 (2016) 623–629.

[50] X. Xiao, C.-T. He, S. Zhao, J. Li, W. Lin, Z. Yuan, Q. Zhang, S. Wang, L. Dai, D. Yu, A general approach to cobalt-based homobimetallic phosphide ultrathin nanosheets for highly efficient oxygen evolution in alkaline media, Energy Environ. Sci. 10 (2017) 893–899.

[51] J. Cao, C. Lei, J. Yang, X. Cheng, Z. Li, B. Yang, X. Zhang, L. Lei, Y. Hou, K. Ostrikov, An ultrathin cobalt-based zeolitic imidazolate framework nanosheet array with a strong synergistic effect towards the efficient oxygen evolution reaction, J. Mater. Chem. A 6 (2018) 18877–18883.

[52] G. Wei, Z. Zhou, X. Zhao, W. Zhang, C. An, Ultrathin metal–organic framework nanosheet-derived ultrathin Co$_3$O$_4$ nanomeshes with robust oxygen-evolving performance and asymmetric supercapacitors, ACS Appl. Mater. Interfaces 10 (2018) 23721–23730.

[53] G. Li, X. Zhang, H. Zhang, C. Liao, G. Jiang, Bottom-up MOF-intermediated synthesis of 3D hierarchical flower-like cobalt-based homobimetallic phophide composed of ultrathin nanosheets for highly efficient oxygen evolution reaction, Appl. Catal. B: Environ. 249 (2019) 147–154.

[54] M. Huang, W. Liu, L. Wang, J. Liu, G. Chen, W. You, J. Zhang, L. Yuan, X. Zhang, R. Che, Self-transforming ultrathin α-Co(OH)$_2$ nanosheet arrays from metal-organic framework modified graphene oxide with sandwichlike structure for efficient electrocatalytic oxygen evolution, Nano Res. 13 (2020) 810–817.

[55] C. Wen, L. Chen, Y. Xie, J. Bai, X. Liang, MOF-derived carbon-containing Fe doped porous CoP nanosheets towards hydrogen evolution reaction and hydrodesulfurization, Int. J. Hydrog. Energy 46 (2021) 33420–33428.

[56] G. Li, H. Kobayashi, J.M. Taylor, R. Ikeda, Y. Kubota, K. Kato, M. Takata, T. Yamamoto, S. Toh, S. Matsumura, H. Kitagawa, Hydrogen storage in Pd nanocrystals covered with a metal–organic framework, Nat. Mater. 13 (2014) 802–806.

[57] J.D. Nguyen, B.S. Matsuura, C.R.J. Stephenson, A photochemical strategy for lignin degradation at room temperature, J. Am. Chem. Soc. 136 (2014) 1218–1221.

[58] H. Luo, L. Wang, S. Shang, G. Li, Y. Lv, S. Gao, W. Dai, Cobalt nanoparticles-catalyzed widely applicable successive C—C bond cleavage in alcohols to access esters, Angew. Chem. Int. Ed. 59 (2020) 19268–19274.

[59] R. Wei, X. Qu, Y. Xiao, J. Fan, G. Geng, L. Gao, G. Xiao, Hydrogenolysis of glycerol to propanediols over silicotungstic acid catalysts intercalated with CuZnFe hydrotalcite-like compounds, Catal. Today 368 (2021) 224–231.

[60] B. Ravel, M. Newville, Athena, Artemis, Hephaestus: data analysis for X-ray absorption spectroscopy using IFEFFIT, J. Synchrotron Radiat. 12 (2005) 537–541.

[61] S.I. Zabinsky, J.J. Rehr, A. Ankudinov, R.C. Albers, M.J. Eller, Multiple-scattering calculations of x-ray-absorption spectra, Phys. Rev. B 52 (1995) 2995–3009.

[62] H. Funke, A.C. Scheinost, M. Chukalina, Wavelet analysis of extended x-ray absorption fine structure data, Phys. Rev. B 71 (2005), 094110.

[63] B. Lim, M. Jiang, J. Tao, P.H.C. Camargo, Y. Zhu, Y. Xia, Shape-controlled synthesis of pd nanocrystals in aqueous solutions, Adv. Funct. Mater. 19 (2009) 189–200.

[64] H.-C. Peng, S. Xie, J. Park, X. Xia, Y. Xia, Quantitative analysis of the coverage density of Br⁻ ions on Pd{100} facets and its role in controlling the shape of Pd nanocrystals, J. Am. Chem. Soc. 135 (2013) 3780–3783.

[65] X. Li, Y. Pan, H. Yi, J. Hu, D. Yang, F. Lv, W. Li, J. Zhou, X. Wu, A. Lei, L. Zhang, Mott–Schottky effect leads to alkyne semihydrogenation over Pd-Nanocube@N-doped carbon, ACS Catal. 9 (2019) 4632–4641.

[66] M. Jin, H. Liu, H. Zhang, Z. Xie, J. Liu, Y. Xia, Synthesis of Pd nanocrystals enclosed by {100} facets and with sizes <10 nm for application in CO oxidation, Nano Res. 4 (2011) 83–91.

[67] Q. Yang, Q. Xu, S.-H. Yu, H.-L. Jiang, Pd Nanocubes@ZIF-8: integration of plasmon-driven photothermal conversion with a metal–organic framework for efficient and selective catalysis, Angew. Chem. Int. Ed. 55 (2016) 3685–3689.

[68] J. Yang, F. Zhang, H. Lu, X. Hong, H. Jiang, Y. Wu, Y. Li, Hollow Zn/Co ZIF particles derived from core–shell ZIF-67@ZIF-8 as selective catalyst for the semi-hydrogenation of acetylene, Angew. Chem. Int. Ed. 54 (2015) 10889–10893.

[69] Y. Li, S.L. Zhang, W. Cheng, Y. Chen, D. Luan, S. Gao, X.W. Lou, Loading single-Ni atoms on assembled hollow N-rich carbon plates for efficient CO$_2$ electroreduction, Adv. Mater. 34 (2022) 2105204.

[70] G. Lu, S. Li, Z. Guo, O.K. Farha, B.G. Hauser, X. Qi, Y. Wang, X. Wang, S. Han, X. Liu, J.S. DuChene, H. Zhang, Q. Zhang, X. Chen, J. Ma, S.C.J. Loo, W.D. Wei, Y. Yang, J.T. Hupp, F. Huo, Imparting functionality to a metal–organic framework material by controlled nanoparticle encapsulation, Nat. Chem. 4 (2012) 310–316.

[71] X. Zhang, L. Chang, Z. Yang, Y. Shi, C. Long, J. Han, B. Zhang, X. Qiu, G. Li, Z. Tang, Facile synthesis of ultrathin metal-organic framework nanosheets for Lewis acid catalysis, Nano Res. 12 (2019) 437–440.

[72] J. Cheng, H. Guo, X. Yang, Y. Mao, L. Qian, Y. Zhu, W. Yang, Phosphotungstic acid-modified zeolite imidazolate framework (ZIF-67) as an acid-base bifunctional heterogeneous catalyst for biodiesel production from microalgal lipids, Energy Convers. Manag. 232 (2021), 113872.

[73] Y. Qu, A. Wu, Y. Jiao, H. Zheng, X. Wang, Y. Xie, L. Wang, C. Tian, H. Fu, Two-dimensional porous molybdenum phosphide/nitride heterojunction nanosheets for pH-universal hydrogen evolution reaction, Angew. Chem. Int. Ed. 60 (2021) 6673–6681.

[74] K. Li, B. Zhao, H. Zhang, H. Lv, J. Bai, H. Ma, P. Wang, W. Li, J. Si, X. Zhu, Y. Sun, 3D porous honeycomb-like CoN-Ni$_3$N/N-C nanosheets integrated electrode for high-energy-density flexible supercapacitor, Adv. Funct. Mater. 31 (2021) 2103073.

[75] J. Ji, K. Deng, J. Li, Z. Zhang, X. Duan, H. Huang, In situ transformation of 3D Co$_3$O$_4$ nanoparticles to 2D nanosheets with rich surface oxygen vacancies to boost hydrogen generation from NaBH$_4$, Chem. Eng. J. 424 (2021), 130350.

[76] Y. Ren, Y. Zou, Y. Liu, X. Zhou, J. Ma, D. Zhao, G. Wei, Y. Ai, S. Xi, Y. Deng, Synthesis of orthogonally assembled 3D cross-stacked metal oxide semiconducting nanowires, Nat. Mater. 19 (2020) 203–211.

[77] M. Zhou, J. Guo, B. Zhao, C. Li, L. Zhang, J. Fang, Improvement of oxygen reduction performance in alkaline media by tuning phase structure of Pd–Bi nanocatalysts, J. Am. Chem. Soc. 143 (2021) 15891–15897.

[78] T. Rajkumar, G. Ranga, Rao, Synthesis and characterization of hybrid molecular material prepared by ionic liquid and silicotungstic acid, Mater. Chem. Phys. 112 (2008) 853–857.

[79] H. Gong, Z. Wei, Z. Gong, J. Liu, G. Ye, M. Yan, J. Dong, C. Allen, J. Liu, K. Huang, R. Liu, G. He, S. Zhao, H. Fei, Low-coordinated Co-N-C on oxygenated graphene for efficient electrocatalytic H$_2$O$_2$ production, Adv. Funct. Mater. 32 (2022) 2106886.

[80] K. Kojima, R. Osuga, S. Yasuda, T. Yokoi, Y. Hosogi, S. Itagaki, Y. Okumura, J. N. Kondo, Characterization of H$_4$SiW$_{12}$O$_{40}$ supported on mesoporous silica (SBA-15), non-structured amorphous silica and γ-alumina, J. Catal. 395 (2012) 387–398.

[81] S. Zhu, X. Gao, Y. Zhu, Y. Zhu, X. Xiang, C. Hu, Y. Li, Alkaline metals modified Pt–H$_4$SiW$_{12}$O$_{40}$/ZrO$_2$ catalysts for the selective hydrogenolysis of glycerol to 1,3-propanediol, Appl. Catal. B: Environ. 140–141 (2013) 60–67.

[82] B.H. Davis, R.A. Keogh, S. Alerasool, D.J. Zalewski, D.E. Day, P.K. Doolin, Infrared study of pyridine adsorbed on unpromoted and promoted sulfated zirconia, J. Catal. 183 (1999) 45–52.

[83] K. Zhou, B. Mousavi, Z. Luo, S. Phatanasri, S. Chaemchuen, F. Verpoort, Characterization and properties of Zn/Co zeolitic imidazolate frameworks vs. ZIF-8 and ZIF-67, J. Mater. Chem. A 5 (2017) 952–957.

[84] M. Wang, H. Shi, D.M. Camaioni, J.A. Lercher, Palladium-catalyzed hydrolytic cleavage of aromatic C—O bonds, Angew. Chem. Int. Ed. 56 (2017) 2110–2114.

[85] M. Zhou, C. Tang, J. Li, H. Xia, P. Liu, J. Xu, C. Chen, J. Jiang, Spherical NiCo-MOFs catalytic hydrogenolysis of lignin dimers and enzymatic lignin to value-added liquid fuels under nitrogen atmosphere, Fuel 315 (2022), 123156.

[86] W. Lan, J.B. deBueren, J.S. Luterbacher, Highly selective oxidation and depolymerization of α,γ-diol-protected lignin, Angew. Chem. Int. Ed. 58 (2019) 2649–2654.

[87] K. Alharbi, W. Alharbi, E.F. Kozhevnikova, I.V. Kozhevnikov, Deoxygenation of ethers and esters over bifunctional Pt–heteropoly acid catalyst in the gas phase, ACS Catal. 6 (2016) 2067–2075.